Available online at www.sciencedirect.com

ScienceDirect

Underground Space 26 (2026) 152–174

www.keaipublishing.com/undsp

Research Paper

Response law of rock-cutterhead interaction in intact sandstone through TBM tunnelling test

Weiqiang Xie [a,b], Xiaoli Liu [a,b,*], Caifeng Zhang [a], Xiaoxiong Zhou [a,d], Jian Chen [c]

[a] State Key Laboratory of Hydroscience and Engineering, Tsinghua University, Beijing 100084, China
[b] Yunlong Lake Laboratory of Deep Underground Science and Engineering, Xuzhou 221000, China
[c] Rugao Yuanye Survey Machinery Factory, Rugao 226531, China
[d] School of Civil Engineering, Chongqing Jiaotong University, Chongqing 400074, China

Received 25 January 2025; received in revised form 18 April 2025; accepted 10 June 2025
Available online 24 October 2025

Abstract

The unclear response law of rock-cutterhead interaction seriously limits the tunnel boring machine (TBM) efficiency. Various influencing factors make it difficult to illustrate the law using the TBM tunnelling results in the field. In the present study, we develop a novel TBM tunnelling test platform (DGTBM-A) to analyze rock-cutterhead interaction. The components and functions of the platform are introduced. The cubic sandstone specimens (500 mm × 500 mm × 500 mm) with three distinct uniaxial compressive strengths (low (24.94 MPa), medium (61.22 MPa), and high (95.04 MPa) are used for TBM tunnelling test. The effects of cutterhead thrust, rotational speed and rock strength on the rock-cutterhead interaction are examined. Key tunnelling parameters, TBM performance indices, and rock muck characteristics are analyzed to reflect their effects. The findings revealed significant impacts of cutterhead thrust, rotational speed and rock strength on torque, advance rate, penetration rate, specific energy, and field penetration index. Additionally, the characteristics of the produced rock muck varied with the applied tunnelling parameters, providing insights into the efficiency and effectiveness of rock breaking. Correlations between the TBM performance indices and the influencing factors are established. The results contribute to a better understanding of the mechanics involved in TBM tunnelling in sandstone, aiding in optimizing operational parameters for improved performance and cost-efficiency in engineering practice.

Keywords: Tunnel boring machine; Rock-cutterhead interaction; Tunnelling test platform; Sandstone

1 Introduction

Tunnel boring machines (TBMs) are critical for advancing tunnelling projects efficiently, especially in challenging geological conditions (Barton, 2000; Feng et al., 2021; Ma et al., 2020; Wijk, 1992). Understanding the interaction between the rock and the cutterhead of a TBM is fundamental to optimizing tunnelling performance and minimizing wear and tear on equipment (Gong et al., 2016; Rostami, 2016; Yagiz, 2008). Much research has focused on revealing the rock-cutterhead interaction using field data or simulation data (Hassanpour et al., 2020; Heydari et al., 2019; Khetwal et al., 2020; Wu et al., 2019). There remains a need for comprehensive studies on the response law of rock-cutterhead interaction in intact sandstone specimens through TBM tunnelling test.

Sandstone, known for its varying degrees of strength and abrasiveness, presents unique challenges and opportunities in TBM tunnelling (Bejari, 2013; Goodarzi et al., 2021; Nouri et al., 2022; Zou et al., 2020). The interaction between the TBM cutterhead and sandstone can significantly affect tunnelling efficiency, cutter wear, and overall project cost. Therefore, it is essential to understand how different operational parameters, including the thrust and

* Corresponding author at: State Key Laboratory of Hydroscience and Engineering, Tsinghua University, Beijing 100084, China.
E-mail address: xiaoli.liu@tsinghua.edu.cn (X. Liu).
Peer review under the responsibility of Tongji University

https://doi.org/10.1016/j.undsp.2025.06.006

rotational speed, influence the performance and durability of TBM components in sandstone environments.

Great number of tunnelling data can be recorded by the TBM during the continuous tunnelling process (Li et al., 2023b; Mostafa et al., 2024; Pan et al., 2022; Zhang et al., 2019). These data are commonly used to evaluate TBM performance and rock mass condition using artificial intelligence technologies (Armaghani et al., 2024; Hou et al., 2022). Some potential relationships of rock-cutterhead interaction have been obtained using the data of TBM tunnelling. For instance, the rock mass classification can be predicted according to the tunnelling parameters (Gong et al., 2021a; Hou et al., 2022; Salimi et al., 2019). However, it is worth noting that the data preprocessing is time-consuming. The computer algorithms and input index that applied seriously influence the accuracy of the model. Furthermore, the connections between the input and output parameters using big data are ambiguous (Chen et al., 2020; Li et al., 2023a; Zhang et al., 2019).

Essentially, the TBM tunnelling process is an interaction of rock/rockmass and cutterhead, where rock/rockmass is broken into blocks (Gong et al., 2022; Wu et al., 2021; Xie et al., 2021). Both the TBM condition and rock condition influence the response characteristics. Thus, the experimental study is another method to investigate the rock-cutterhead interaction (Feng et al., 2024; Lee & Kwon, 2023; Tang et al., 2024). Wang et al. (2024b) investigated the wear behavior of TBM cutter rings under different tunnelling parameters using rock-like material. Some researchers have carried out physical model tests to investigate the rock-cutterhead interaction (Feng et al., 2024; Fu et al., 2024; Wang et al., 2024a). The rock conditions (such as strength and stress) and TBM conditions (such as cutter design and tunnelling parameters) can be available in these physical model tests. However, the existing physical model tests have the following limitations. Firstly, the test apparatuses cannot break the rock specimen or break the specimen continuously. The cutterhead in these apparatuses frequently rubs on the rock surface (Feng et al., 2024). Secondly, the tested specimens are rock-like material (Wang et al., 2023), rather than actual rock. Thirdly, the cutterhead design is different from the actual TBM cutterhead (Fu et al., 2024). The existing test platform cannot simulate the tunnelling process correctly. The obtained tunnelling test results may differ from the actual response law of rock-cutterhead interaction in TBM tunnelling. Thus, it is significantly necessary to develop a novel tunnelling test platform for rock-cutterhead interaction analysis.

This study aims to investigate the response characteristics of rock-cutterhead interaction when TBM drives in intact sandstone specimens. To realize this goal, we developed a novel tunnelling test platform (DGTBM-A) to carry out a tunnelling test. The components and functions of the platform are introduced. The cubic sandstone specimens (500 mm × 500 mm × 500 mm) with three distinct uniaxial compressive strengths (low, medium, high, 24.94-61.22-95.04 MPa) are used for TBM tunnelling tests. A total of 24 tunnelling tests are carried out to examine the effects of cutterhead thrust, rotational speed, and rock strength on the rock-cutterhead interaction. These effects are reflected by the key tunnelling parameters, TBM performance indices, and rock muck characteristics. Correlations between the TBM performance and influencing factors are established. The tunnelling test results are validated by the theoretical analysis of rock-cutter interaction. The findings provide valuable insights into optimizing TBM operations and enhancing the efficiency of tunnelling projects in sandstone formations.

2 Methods and materials

This section illustrates the used methods and rock specimens. A tunnelling test platform for rock-cutterhead interaction in TBM is proposed. The components and functions of the platform are introduced. The physical and mechanical properties of the sandstone specimens are obtained. Then the testing schemes are presented for the study of rock-cutterhead interaction.

2.1 TBM tunnelling test platform

We developed a novel tunnelling test platform (DGTBM-A) for the analysis of rock-machine interaction during the TBM tunnelling process (Fig. 1). The DGTBM-A platform is composed of five parts: tunnelling subsystem, hydraulic loading subsystem, sample installation subsystem, control subsystem, and integrated monitoring subsystem. The tunnelling subsystem contains the servomotor, propulsion cylinders, spindle, and cutterhead. The cutterhead contains 18 cutters of different sizes and angles. The integrated monitoring subsystem is equipped with the tunnelling subsystem. It records the thrust, torque, and penetration of the cutterhead in time. The propulsion cylinders are connected with the hydraulic loading subsystem through two oil pipes. These cylinders can move forward/backward to realize the pressurizing/depressurizing conditions by adjusting the directions of the hydraulic oil. The control subsystem is the human–machine interactive operating platform of the equipment. It is connected with the tunnelling subsystem, hydraulic loading subsystem and integrated monitoring subsystem through data cables. The control subsystem controls the whole process of the tunnelling test, as well as records and presents the test results in real-time. More details about the technical parameters of the DGTBM-A platform are listed in Table 1. For more details about the DGTBM-A, the readers can refer to Xie et al. (2025).

To exclude the possible influence of the operator, the tunnelling tests using the DGTBM-A platform should be performed according to the following routine procedures.

Step 1: Specimen installation. The top plate of the model box is removed by the gantry crane. Then the cubic specimen is placed in the box using two lifting slings. These two

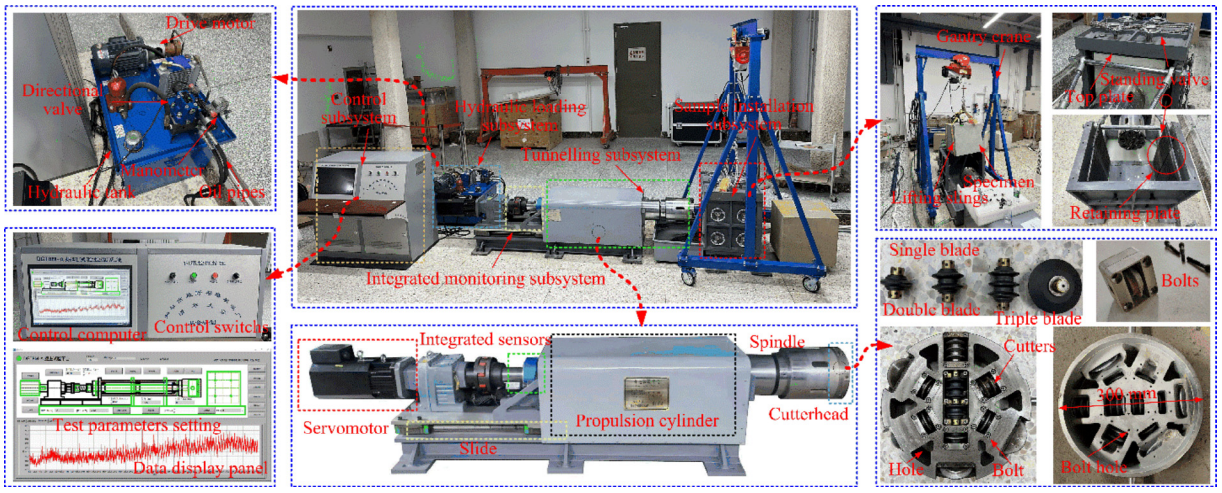

Fig. 1. Components of the DGTBM-A platform for TBM tunnelling test.

Table 1
Technical parameters of the novel TBM tunnelling test platform.

Technical parameter	Design value
Total weight of the platform (kg)	2000
Dimensions of the platform (mm × mm × mm)	Approx. 6000 × 1000 × 1000
Number of normal cutters	18
Excavation diameter (mm)	≥300
Maximum loading force (kN)	200
Maximum torque (N•m)	1670
Maximum penetration (mm)	430
Loading control type	Force control/penetration control
Rotational speed (r/min)	1–100
Cutterhead power (kW)	15.6
Specimen size (mm × mm × mm)	500 × 500 × 500
Force accuracy (kN)	0.01
Penetration accuracy (mm)	0.01
Sampling frequency (Hz)	10

slings should be removed when the rock specimen is in place. Afterwards, the top plate is placed in place using the gantry crane. All the standing valves are tightened to fix the rock specimen.

Step 2: Turn on the switches. There are four switches on the human–machine interactive operating platform (Fig. 1). The black knob switch on the left is the platform's main power switch. The green and red buttons are the switches that turn the control subsystem on and off, respectively. The black knob switch on the right is the switch of the servomotor. Firstly, open the software on the control computer. Then turn on the black knob switch on the right to rotate the cutterhead. Finally, turn on the green button to prepare the hydraulic loading subsystem for pressurization or pressure relief.

Step 3: Set the parameters for the tunnelling test. Firstly, select the control type. There are two types of tunnelling control: thrust control and advance rate control. Secondly, set the tunnelling parameters according to the designed scheme. The target thrust, advance rate and rotational speed of the cutterhead can be set in the software.

Step 4: Tunnelling test. Firstly, turn on the faucet switch. There is a water nozzle inside the cutterhead. It is connected to an outside water line. Turn on the data acquisition button and the start tunnelling button. The tunnelling subsystem moves forward to excavate the rock specimen. The integrated sensors record the test data and transmit it to the control computer. During the tunnelling test process, the tunnelling parameters can be changed in the selected control types. For example, the target thrust and rotational speed of the cutterhead can be changed in thrust control, and the target advance rate and rotational speed of the cutterhead can be changed in advance rate control. The tunnelling data are presented in the software in real-time. When the designed scheme is finished, turn off the data acquisition button first. Then change the direction of hydraulic oil in and out to back the tunnelling subsystem. Turn off the switch of the servomotor. Finally, turn off the control subsystem and the platform's main power switch.

Step 5: Specimen removal. Firstly, the top plate of the model box should be removed. A lifting ring is fixed to the top surface of the rock specimen. Then the rock specimen is removed through the gantry crane. The produced rock muck during the TBM tunnelling process is collected for further analysis. Next tunnelling test can be carried out by repeating the steps 1–5.

2.2 Sandstone specimens

Sandstone specimens are used in the present study for the consideration of extensiveness and abrasiveness of the rock. Sandstone is frequently present in the geological condition of TBM tunnelling. It has lower abrasiveness compared with granite. Thus, the disc cutters do not need to be replaced frequently. In addition, sandstone specimens

are suitable for TBM tunnelling commissioning work with uncertainty. The sandstones used in the present study are collected from Shandong Province, China. As shown in Fig. 2, large rock blocks are obtained from the open-air rocky mountains through drilling and cutting. Then these large blocks are cut into the designed specimens using the cutting machine. Three cubic sandstone specimens with dimensions of 500 mm × 500 mm × 500 mm, numbered #1, #2, and #3, are used in the present study (Fig. 2). The cutterhead of the DGTBM-A platform has an excavation diameter of 300 mm. The uniaxial compressive strength (UCS) of these sandstone specimens is divided into three classes, i.e., low strength (#1), medium strength (#2), and high strength (#3), and further analysis of the rock strength effect on rock-cutterhead interaction will be illustrated. It is worth explaining that the class of the low, medium, and high is not categorized according to any standard. The low, medium, and high only represent the three different strengths of sandstones used in this study.

Standard core specimens are prepared to obtain the basic physical and mechanical properties of the three cubic sandstone specimens. As shown in Fig. 2(e), three core specimens with a diameter of 50 mm, a height of 100 mm, and three core specimens with a diameter of 50 mm, a height of 25 mm are used for the uniaxial compression test and Brazilian tensile test, respectively. The density, UCS, tensile strength (σ_t), and elastic modulus (E) of the sandstone specimens are acquired using these core specimens. The corresponding tests are carried out according to the methods recommended by the International Society for Rock Mechanics (Ulusay, 2015). Details about these physical and mechanical properties are presented in Table 2. It can be seen that the strength gradient of these sandstone specimens is about 30 MPa (25 MPa–61 MPa–95 MPa), which contains a common UCS of rocks in the geological condition TBM encounters. Parts of the data in uniaxial compression tests were not recorded in specimens #2 and #3 due to the failure of the data acquisition system.

2.3 Tunnelling test schemes

The operating parameters, i.e., thrust (F), rotational speed of cutterhead (n_{rpm}) are frequently adjusted in engineering practice due to the complex geological conditions. Thus, the present study aims to investigate the thrust effect and rotational speed effect on rock-cutterhead interaction through the DGTBM-A platform. The tunnelling parameters (including rotational speed and thrust) are determined through a series of trial tests and theoretical analysis. In a trial test, if the thrust is too low, the sandstone may not be broken. If the rotational speed is too low, the torque may exceed the rated limit. Theoretical analysis is presented in Section 3.4 to validate the tunnelling test results. The tunnelling process is essentially a breaking process of rock-cutterhead interaction. Thus, the rock strength effect on rock-cutterhead interaction is also investigated. To exclude the simultaneous effects of multiple variables, in each sandstone specimen, the rotational speed is kept constant when the thrust is changing, and vice versa. Details about the tunnelling test schemes are presented in Table 3. A total of 24 tunnelling tests (8 tests in each sandstone specimen) are carried out. The tunnelling time of each test is about 150 s (this time is the excavation duration of the stable section). The actual tunnelling time may be changed due to the

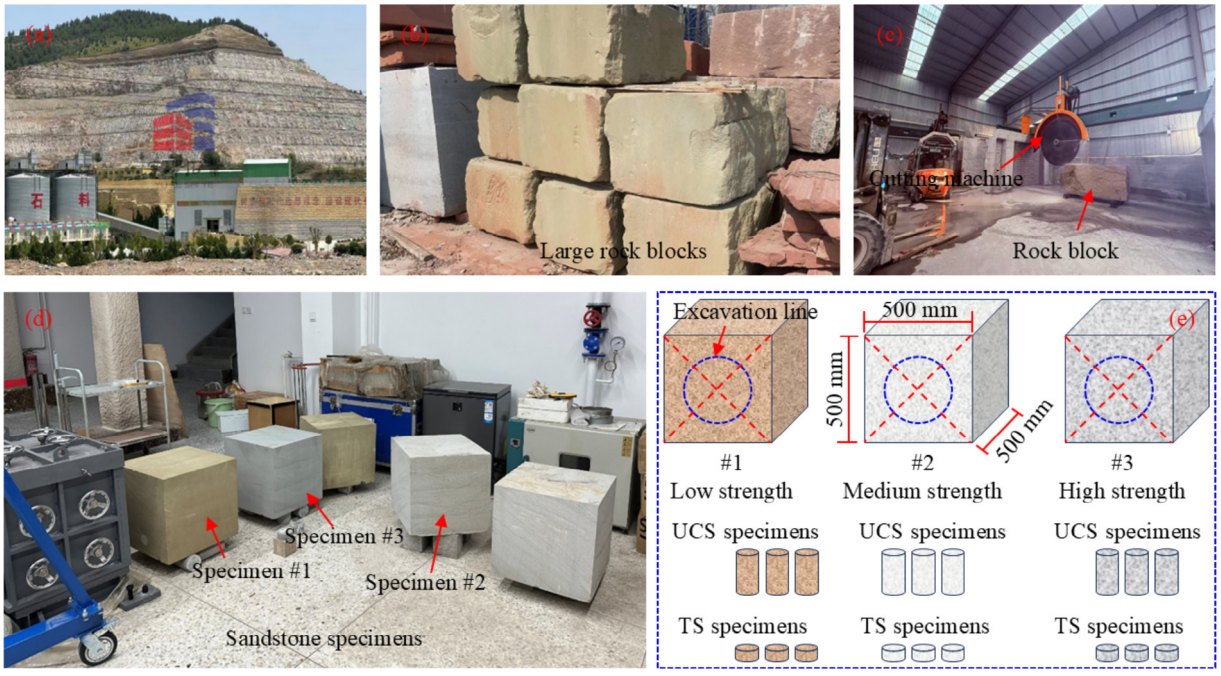

Fig. 2. Acquisition of the intact sandstone specimens for TBM tunnelling test. (a) Collection site in Shandong Province, China, (b) large rock blocks, (c) rock cutting, (d) intact specimens after cutting, and (e) the details about the three sandstone specimens.

Table 2
Physical and mechanical properties of the three intact sandstone specimens.

Specimen No.	Density (kg/cm^3)		UCS (MPa)		σ_t (MPa)		E (GPa)	
	Tested value	Average	Tested value	Average	Tested value	Average	Tested value	Average
#1	2238.11	2238.11	26.00	24.94	2.21	2.12	2.20	2.86
	2238.11		23.32		2.19		2.93	
	2238.11		25.51		1.96		3.45	
#2	2652.58	2652.58	63.32	61.22	5.06	4.23	10.38	10.38
	2652.58		65.34		4.17		–	
	2652.58		55.00		3.45		10.37	
#3	2873.63	2873.63	90.27	95.04	9.01	6.81	13.90	15.11
	2873.63		112.08		5.91		–	
	2873.63		82.78		5.50		16.31	

following reasons. (1) The remaining distance of the sandstone specimen or the penetration is insufficient to complete the 150 s of tunnelling. (2) The cutterhead torque exceeds the rated torque. (3) An emergency occurs during the tunnelling process.

3 Results and discussions

According to the tunnelling test schemes, 24 tests are carried out using the three intact sandstone specimens. The response law of rock-cutterhead interaction is analyzed from three aspects in the present study, i.e., thrust effect, rotational speed effect, and rock strength effect. Both the machine condition and rock condition have an impact on the test results. In the following subsections, the response characteristics of tunnelling parameters, performance indices, and rock muck are discussed.

3.1 Thrust effect on rock-cutterhead interaction

3.1.1 Dynamic response of tunnelling parameters

Different thrusts with a gradient of 10 kN are applied to the sandstone specimens to simulate the operational tunnelling thrust in engineering practice. The tunnelling parameters, including thrust, torque, and penetration, are recorded in tunnelling time, as shown in Fig. 3. Due to the different UCS of sandstone specimens, the thrust range is also different. The cutterhead thrust of low-strength rock specimens is 20–50 kN. The cutterhead thrust of medium-strength and high-strength rock specimens is 40–70 kN. The thrust, as one of the key control parameters in rock breaking, has a great impact on TBM tunnelling. Overall, as the thrust increases, the cutterhead torque also increases. The trend of the torque is almost synchronous with that of the thrust. The change of penetration presents a multi-segment linear increase. Each cycle of the TBM tunnelling process can be divided into the rising section and stabilizing section (Chen et al., 2020; Feng et al., 2021). After setting the thrust, the hydraulic loading subsystem raises the thrust to the set value gradually (i.e., the rising section). At the same time, a larger torque is required to rotate the cutterhead at the same rotational speed (Xu et al., 2024); thus, the cutterhead torque gradually increases. It is not difficult to find that the thrust is still in a fluctuating status after reaching the stabilizing section. Generally, the stage from the change of the thrust to the set value is regarded as the rising section in TBM tunnelling, and the advancement after reaching the set value is regarded as the stabling section. It can be seen that the penetration increases in the rising section and changes faster and faster. After reaching the stabling section, the penetration increases at a stable rate (linear increase).

Table 3
Tunnelling test schemes of the three sandstone specimens for rock-cutterhead interaction analysis.

Specimen No.	Test No.	Thrust effect scheme	Test No.	Rotational speed effect scheme
#1	LS-F-1	F = 20 kN, n_{rpm} = 6 r/min	LS-R-1	n_{rpm} = 6 r/min, F = 40 kN
	LS-F-2	F = 30 kN, n_{rpm} = 6 r/min	LS-R-2	n_{rpm} = 10 r/min, F = 40 kN
	LS-F-3	F = 40 kN, n_{rpm} = 6 r/min	LS-R-3	n_{rpm} = 14 r/min, F = 40 kN
	LS-F-4	F = 50 kN, n_{rpm} = 6 r/min	LS-R-4	n_{rpm} = 18 r/min, F = 40 kN
#2	MS-F-1	F = 40 kN, n_{rpm} = 10 r/min	MS-R-1	n_{rpm} = 6 r/min, F = 50 kN
	MS-F-2	F = 50 kN, n_{rpm} = 10 r/min	MS-R-2	n_{rpm} = 10 r/min, F = 50 kN
	MS-F-3	F = 60 kN, n_{rpm} = 10 r/min	MS-R-3	n_{rpm} = 14 r/min, F = 50 kN
	MS-F-4	F = 70 kN, n_{rpm} = 10 r/min	MS-R-4	n_{rpm} = 18 r/min, F = 50 kN
#3	HS-F-1	F = 40 kN, n_{rpm} = 10 r/min	HS-R-1	n_{rpm} = 6 r/min, F = 50 kN
	HS-F-2	F = 50 kN, n_{rpm} = 10 r/min	HS-R-2	n_{rpm} = 10 r/min, F = 50 kN
	HS-F-3	F = 60 kN, n_{rpm} = 10 r/min	HS-R-3	n_{rpm} = 14 r/min, F = 50 kN
	HS-F-4	F = 70 kN, n_{rpm} = 10 r/min	HS-R-4	n_{rpm} = 18 r/min, F = 50 kN

Note: in the test No., LS-low strength, MS-medium strength, HS-high strength, F represents the thrust effect scheme, n_{rpm} represents the rotational speed effect scheme, and numbers are the testing numbers.

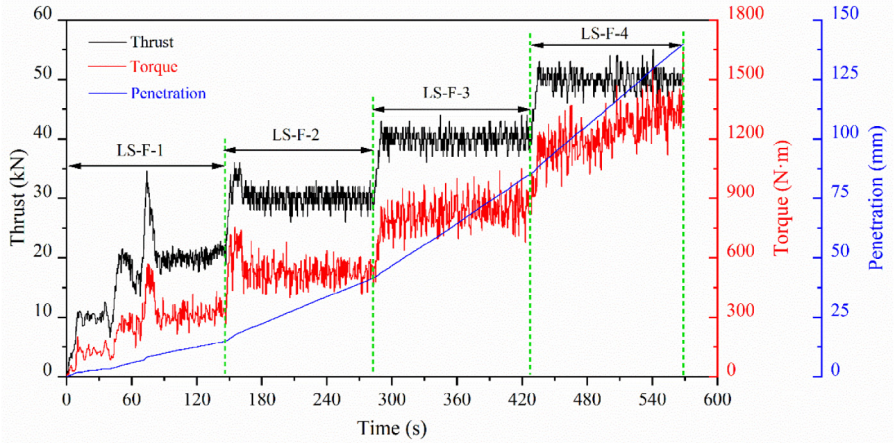

(a)

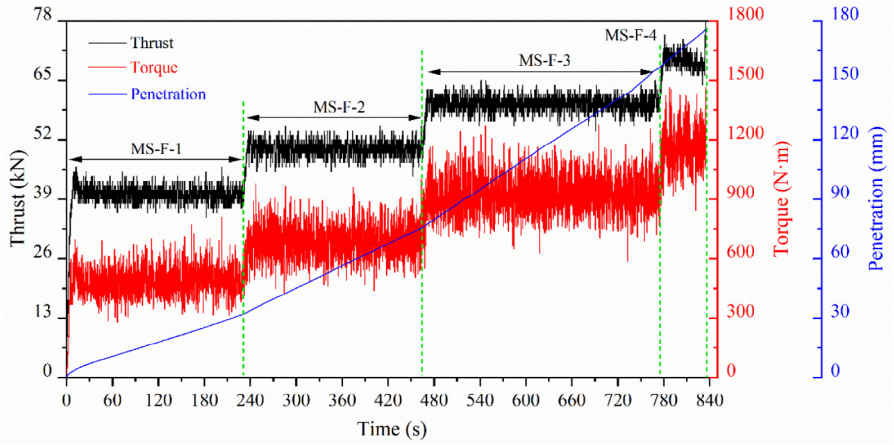

(b)

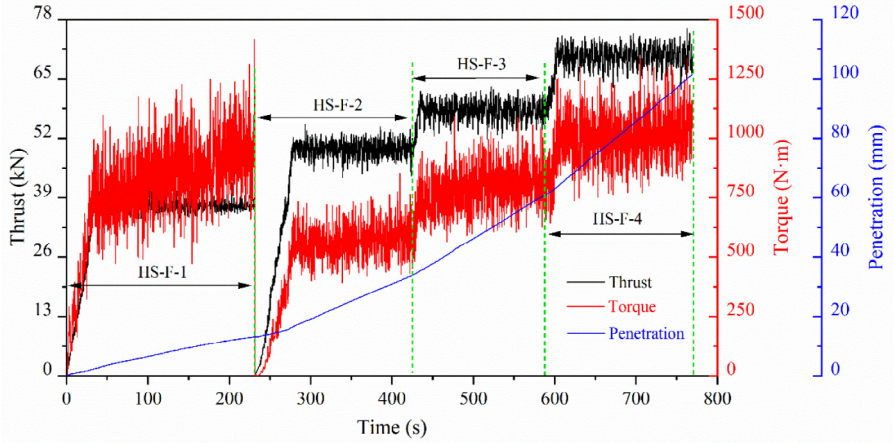

(c)

Fig. 3. Changes of tunnelling parameters under different thrusts during the test process using the three sandstone specimens. (a) Low-strength specimen, (b) medium-strength specimen, and (c) high-strength specimen.

To further illustrate the change of torque during the tunnelling test, the torque in the stabling section under each thrust is statistically analyzed, as shown in Fig. 4. As the thrust increases, the torque increases significantly. When the thrust is 40 kN, the torque required for excavation in high-strength rock specimens is greater than the torque required for the thrust of 50 kN. The reason is that the cutters on the cutterhead in 40 kN thrust have been severely worn (Fig. 4(d)), resulting in the increase of torque. Then the worn cutters are replaced by new cutters subsequently. This is also the reason why the tunnelling test with a thrust of 50 kN in Fig. 3(c) starts from zero. In addition, the box

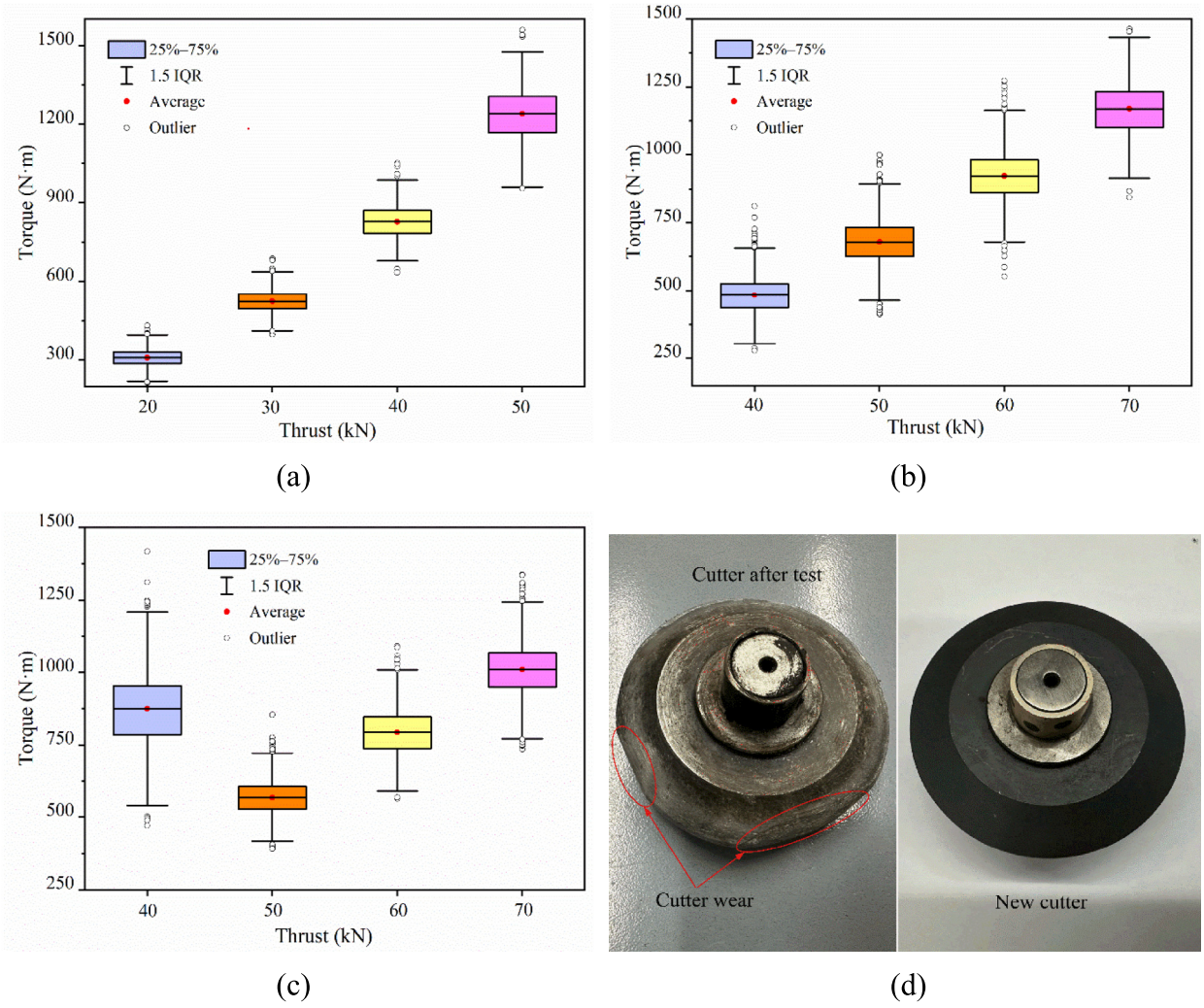

Fig. 4. Box plots of cutterhead torque under different thrusts using the three sandstone specimens. (a) Low-strength specimen, (b) medium-strength specimen, (c) high-strength specimen, and (d) the worn cutter after test and the new cutter.

Table 4
Averages of the TBM performance indices calculated from the stabilizing section in different thrusts.

Test No.	Variable (kN)	T (N·m)	v (mm/min)	p_r (mm/r)	E_s (MJ/m^3)	I_{fp} (kN·rev/mm)
LS-F-1	20	309.10	5.22	0.87	0.28	1.28
LS-F-2	30	524.11	11.32	1.89	0.42	0.88
LS-F-3	40	828.00	18.14	3.02	0.57	0.74
LS-F-4	50	1239.1	23.24	3.87	0.71	0.72
MS-F-1	40	482.62	7.52	0.75	0.57	2.96
MS-F-2	50	679.83	11.26	1.13	0.71	2.46
MS-F-3	60	922.10	15.60	1.56	0.85	2.13
MS-F-4	70	1168.6	19.34	1.93	0.98	1.99
HS-F-1	40	873.56	3.42	0.34	0.57	6.54
HS-F-2	50	568.08	7.11	0.71	0.71	3.91
HS-F-3	60	793.36	10.08	1.01	0.85	3.30
HS-F-4	70	1009.0	13.55	1.36	0.98	2.86

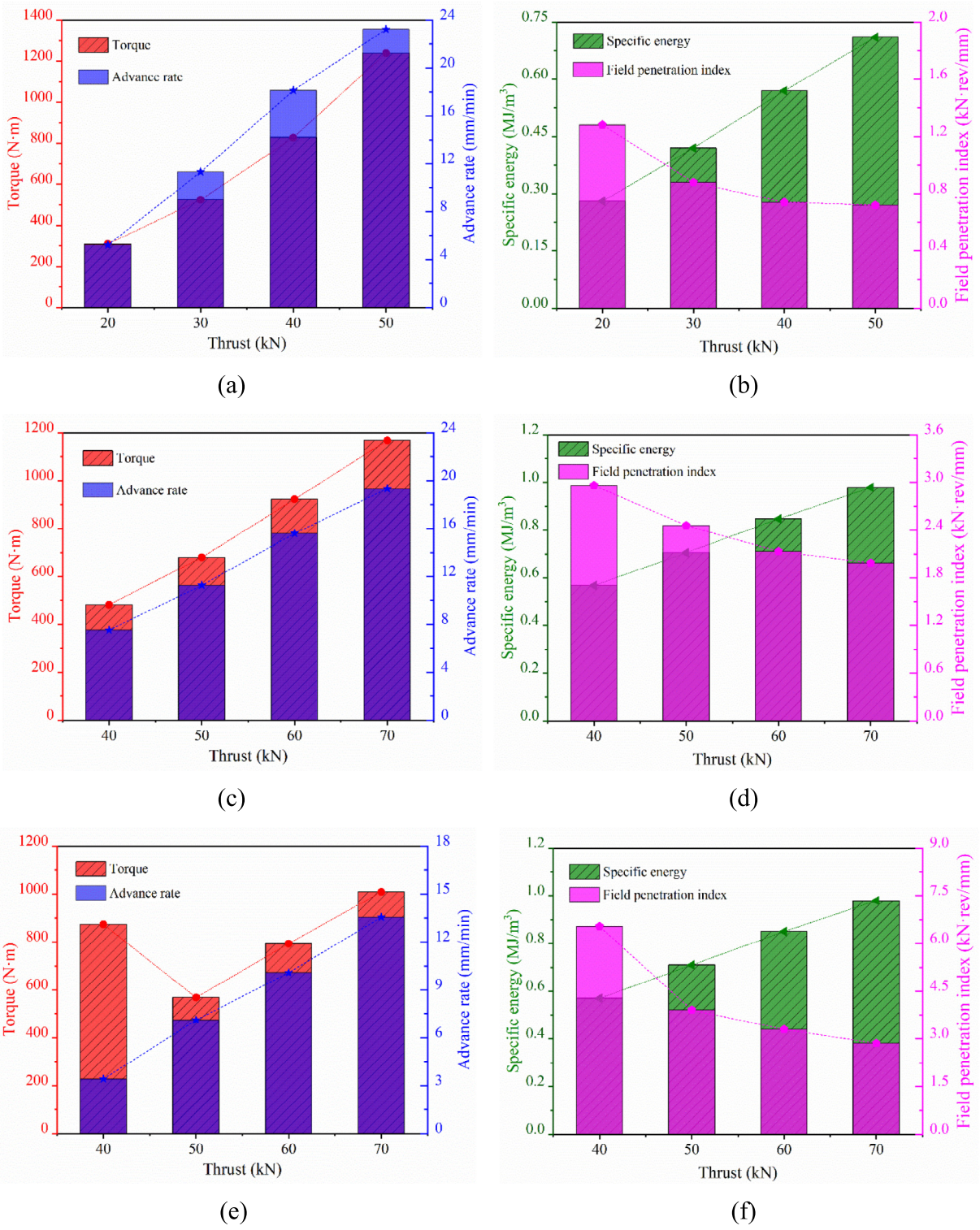

Fig. 5. Thrust effect on the torque and TBM performance indices using the three sandstone specimens with different strengths, including (a)–(b) low strength, (c)–(d) medium strength, and (e)–(f) high strength.

plots show that as the thrust increases, the box height (25%–75%) increases, i.e., the fluctuation range of the torque increases. The thrust and the torque show an obvious positive correlation.

3.1.2 Response law of TBM performance

The TBM performance reflects the TBM conditions in the rock breaking process. In order to further quantify the TBM performance during the tunnelling process, the

Table 5
Quantitative relationship models of the thrust effect on the torque and TBM performance indices.

Rock strength class	Index for TBM tunnelling	Model	R^2
Low strength	Torque	$T = 30.94F - 357.78$	0.980
	Advance rate	$v = 0.61F - 6.83$	0.997
	Penetration rate	$p_r = 0.10F - 1.13$	0.997
	Specific energy	$E_s = 0.01F - 0.01$	1.000
	Field penetration index	$I_{fp} = 8.51F^{-0.648}$	0.951
Medium strength	Torque	$T = 23.00F - 451.83$	0.997
	Advance rate	$v = 0.40F - 8.46$	0.999
	Penetration rate	$p_r = 0.04F - 0.84$	0.999
	Specific energy	$E_s = 0.01F + 0.02$	1.000
	Field penetration index	$I_{fp} = 42.22F^{-0.724}$	0.989
High strength	Torque	$T = 22.05F - 532.61$	1.000
	Advance rate	$v = 0.33F - 9.81$	0.998
	Penetration rate	$p_r = 0.03F - 0.99$	0.999
	Specific energy	$E_s = 0.01F + 0.02$	1.000
	Field penetration index	$I_{fp} = 1288.1F^{-1.452}$	0.948

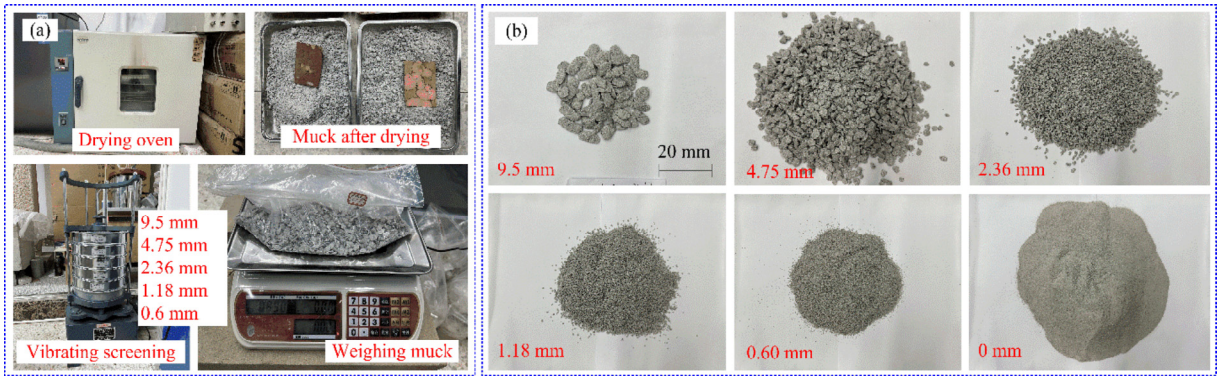

Fig. 6. (a) Acquisition of rock muck information, and (b) an example of muck after screening ($F = 40$ kN, $n_{rpm} = 10$ r/min).

researchers have proposed multiple performance indices (Hassanpour et al., 2015). The commonly used performance indices can be calculated according to Eqs. (1)–(4). These indices in the thrust effect tests are presented in Table 4. It is worth noting that these indices are calculated from the stabilizing section in each test.

$$v = \frac{L}{t}, \tag{1}$$

$$p_r = \frac{v}{n_{rpm}}, \tag{2}$$

$$E_s = \frac{10^{-3} \cdot F \cdot L}{V} = \frac{4 \times 10^{-3} \cdot F}{\pi D^2}, \tag{3}$$

$$I_{fp} = \frac{F}{N \cdot p_r}, \tag{4}$$

where v is the advance rate of cutterhead (mm/min), L is the tunnelling length (m), t is the tunnelling time (s), p_r is the penetration rate of cutterhead (mm/r), n_{rpm} is the rotational speed (r/min), E_s is the specific energy (MJ/m^3), F is the cutterhead thrust (kN), V is the excavated volume (m^3), D is the excavation diameter (m), I_{fp} is the field penetration index (kN·rev/mm), and N is the number of disc cutters, $N = 18$ in the present study. v and p_r are widely used for the evaluation of TBM tunnelling efficiency (Jing et al., 2021; Yu et al., 2024). E_s and I_{fp} are used to evaluate the excavability of rocks as well as the performance of TBMs (Delisio et al., 2013; Hassanpour et al., 2009; Liu et al., 2017).

Figure 5 shows the changes of torque, as well as the TBM performance indices when sandstone specimens of three different strengths are excavated under four different cutterhead thrusts. It shows similar conclusions when TBM drives in these sandstone specimens: as the thrust increases, the cutterhead torque, advance rate, and specific energy increase, and the field penetration index decreases. Combined with the meanings of these performance indices, it can be concluded that the tunnelling efficiency of the TBM and the excavability of sandstone specimens are improved as the thrust increases. At the same time, more energy is required to excavate the same specimen volume. Thus, the selection of TBM tunnelling parameters in engineering practice is a comprehensive consideration of tunnelling efficiency and cost. The quantitative relationship models are established using the test results, as shown in Table 5. All these models have a high coefficient of determination (R^2), namely the performance indices are highly correlated with thrust.

Table 6
Muck information obtained from tunnelling tests with different thrusts and rock specimens.

Test No.	Mass and mass percent of rock muck remaining in the sieve meshes with different diameters (mm)										CI
	$d_s > 9.5$		$4.75 < d_s \leq 9.50$		$2.36 < d_s \leq 4.75$		$1.18 < d_s \leq 2.36$		$0.60 < d_s \leq 1.18$		$d_s \leq 0.60$		
	Weight (kg)	Percent (%)	Weight (kg)	Percent (%)	Weight (kg)	Percent (%)	Weight (kg)	Percent (%)	Weight (kg)	Percent (%)	Weight (kg)	Percent (%)	
LS-F-1	0.08	6.06	0.34	25.76	0.19	14.39	0.07	5.30	0.04	3.03	0.60	45.45	290.15
LS-F-2	0.03	1.12	0.58	21.72	0.35	13.11	0.14	5.24	0.09	3.37	1.48	55.43	245.69
LS-F-3	0.05	1.09	0.84	18.38	0.59	12.91	0.24	5.25	0.15	3.28	2.70	59.08	231.51
LS-F-4	0.03	0.53	0.63	11.03	0.69	12.08	0.30	5.25	0.19	3.33	3.87	67.78	196.85
MS-F-1	0.07	2.17	0.88	27.33	0.44	13.66	0.31	9.63	0.31	9.63	1.21	37.58	290.06
MS-F-2	0.04	0.92	0.64	14.75	0.69	15.90	0.52	11.98	0.55	12.67	1.90	43.78	247.93
MS-F-3	0.08	0.98	1.40	17.20	1.13	13.88	0.82	10.07	0.98	12.04	3.73	45.82	247.54
MS-F-4	0.06	1.16	0.91	17.64	0.66	12.79	0.53	10.27	0.58	11.24	2.42	46.90	246.51
HS-F-1	0.07	5.43	0.46	35.66	0.22	17.05	0.11	8.53	0.07	5.43	0.36	27.91	343.41
HS-F-2	0.11	3.45	1.04	32.60	0.57	17.87	0.29	9.09	0.18	5.64	1.00	31.35	325.08
HS-F-3	0.17	3.62	1.25	26.60	0.86	18.30	0.47	10.00	0.29	6.17	1.66	35.32	305.53
HS-F-4	0.20	2.87	1.99	28.51	1.19	17.05	0.66	9.46	0.43	6.16	2.51	35.96	304.58

3.1.3 Characteristics of rock muck

The rock muck, as the only direct product of rock-cutterhead interaction, can indicate both the TBM conditions and rock conditions (Geng et al., 2019; Gong et al., 2021b; Heydari et al., 2019; Zhou et al., 2021). Thus, in this subsection, the characteristics of muck produced from the tunnelling test are discussed. The muck is collected during each tunnelling test through plastic bags. Then the drying oven is used to dry the muck at 150 °C and 5 h (Fig. 6(a)). The dry muck is sieved into six groups with five sieves (sieve size 9.50, 4.75, 2.36, 1.18 and 0.60 mm). The weight of each group is obtained by the electronic weigher. Figure 6(b) shows an example of muck after sieving. The muck is collected from the tunnelling test with a thrust of 40 kN, a rotational speed of 10 r/min in a medium-strength sandstone specimen. The muck shape tends to be flaky when the muck size is large, and conversely, the muck shape is more compact (closer to spherical) when the muck is small in size. This phenomenon is similar to the results in engineering practice (Xie et al., 2023; Zhang et al., 2021). According to previous studies (Bakar et al., 2014; Gong et al., 2007; Tan et al., 2018), flat rock muck indicates that the rock breaking process of the TBM is effective and efficient. Thus, the results of the tunnelling test reflect the real rock breaking effect in TBM excavation. To further analyze the rock-cutterhead interaction using the muck information, the sieving results are presented in Table 6. The coarseness index (CI) is frequently used to characterize the size distribution of rock muck (Jeong and Jeon, 2018; Tuncdemir et al., 2008). It can be calculated according to Eq. (5). The larger the CI value, the higher the proportion of muck with a large size (Xie et al., 2023).

$$\mathrm{CI} = \sum \frac{w_i}{w_t} \times 100\%, \tag{5}$$

where CI is the coarseness index, w_i is the mass of rock muck remaining on a sieve, and w_t is the total muck mass. The sieve diameters used in the present study are 9.5, 4.75, 2.36, 1.18, and 0.06 mm.

The muck size information screening from different thrusts is statistically analyzed, as shown in Fig. 7. Consistent conclusions can be drawn from the three sandstone specimens with different rock strengths. As the sieve size decreases, the residual mass on the sieve increases first, then decreases, and then increases again. The residual mass on the sieve with a size greater than 9.5 mm accounts for the smallest proportion. The residual mass of powder (sieve size less than 0.6 mm) accounts for the largest proportion. In addition, as the thrust increases, the residual mass of rock muck on the sieve with the same size increases. The test with a thrust of 70 kN in a medium-strength sandstone specimen shows an uneven trend, because its tunnelling time is less than 150 s, resulting in insufficient rock muck collection. Figure 7(d) shows the changes of CI under different thrusts. As the thrust increases, the CI value gradually decreases, i.e., the mass proportion of powder in the rock muck increases. The relationship models between

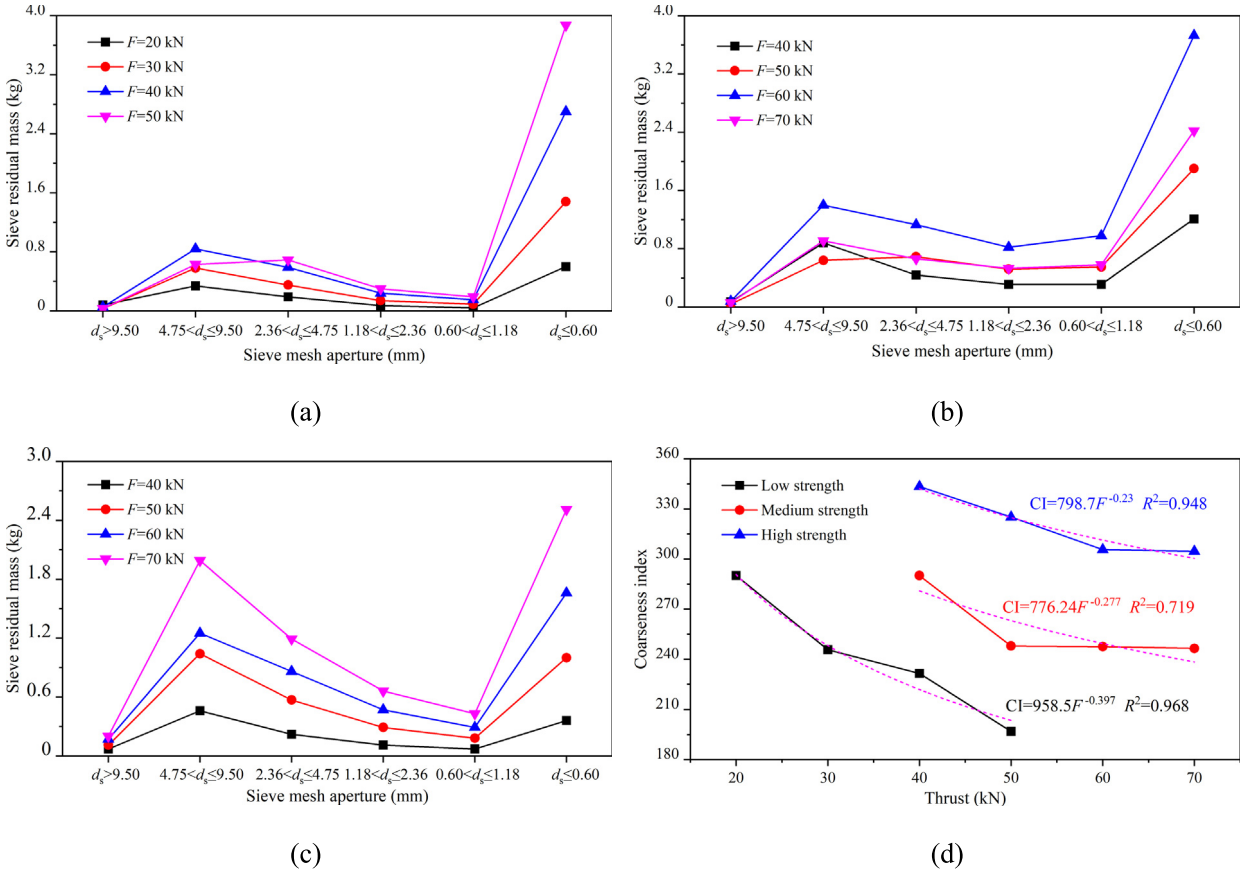

Fig. 7. Muck information collected from the tunnelling tests with different thrusts and sandstone specimens. (a) Low-strength specimen, (b) medium-strength specimen, (c) high-strength specimen, and (d) relationships between coarseness index and thrust.

the CI and thrust are established. These models have high coefficients of determination. They can be used to estimate the tunnelling conditions using rock muck.

3.2 Rotational speed effect on rock-cutterhead interaction

3.2.1 Dynamic response of tunnelling parameters

In this case, the thrust is kept constant, and different rotational speeds with an increase of 4 r/min are applied to the tunnelling tests. The three intact sandstone specimens have different strengths. It is found that the required torque in the low-strength specimen would exceed the rated torque of the test platform if the thrust was set as 50 kN. Thus, the thrust for the low-strength specimen is set as 40 kN. It is not appropriate to set the thrust too large or too small in the excavation of a medium-strength rock specimen. If the thrust is too large, the required torque is likely to exceed the rated torque, and if it is too small, the cutterhead cannot break the rock specimen effectively. If the thrust is set too small for TBM tunnelling in a high-strength specimen, the rock specimen may not be broken by the cutterhead. Finally, the thrust for medium-strength and high-strength specimens is set as 50 kN. The three intact specimens are excavated by the platform at different rotational speeds of 6, 10, 14, and 18 r/min.

Figure 8 shows the changes in tunnelling parameters during the excavation process. The torque is kept at a relatively stable level as the rotational speed changes. The penetration is multi-segment linear, and the growth rate becomes faster, i.e., the tunnelling efficiency is improved as the rotational speed increases. It should be noted that when the TBM drives in the low-strength sandstone specimen, the required torque exceeded the rated torque at the rotational speeds of 10 and 14 r/min. The TBM tunnelling in these conditions is not complete. Also, we found that the slopes of the rising sections (n_{rpm} = 6, 14, 18 r/min) in the low-strength specimen (Fig. 8(a)) are close to each other.

Similarly, the torque in the stabling section under each scheme is statistically analyzed, as shown in Fig. 9. Different trends occur as the rotational speed increases. In a low-strength specimen, the torque increases slightly as the rotational speed increases. The torque of n_{rpm} = 14 r/min is not available due to the incomplete tunnelling. In the medium-strength specimen, the torque decreases slightly with increasing rotational speed, while in high-strength specimen, the torque increases slightly. The torque decreases slightly when the rotational speed is 10 r/min. On the one hand, different rock strengths affect the required torque in the rock-breaking process of TBM excavation. On the other

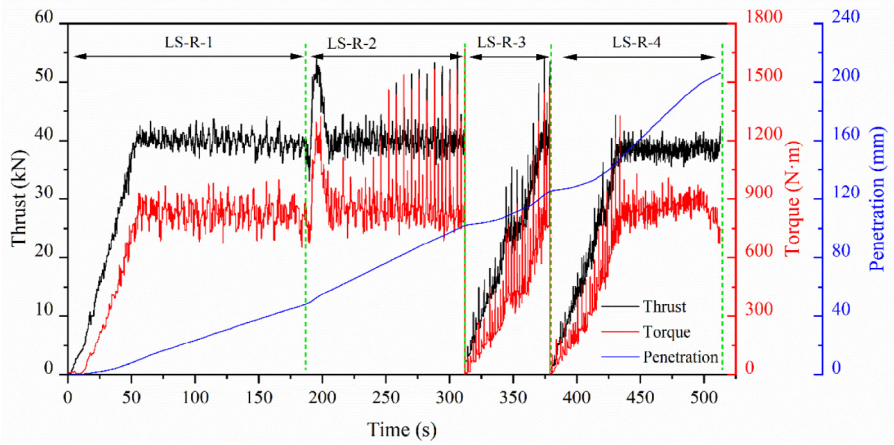

(a)

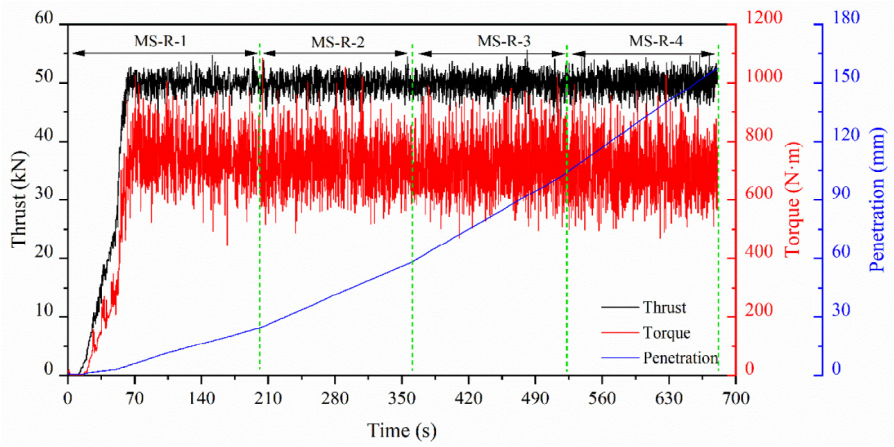

(b)

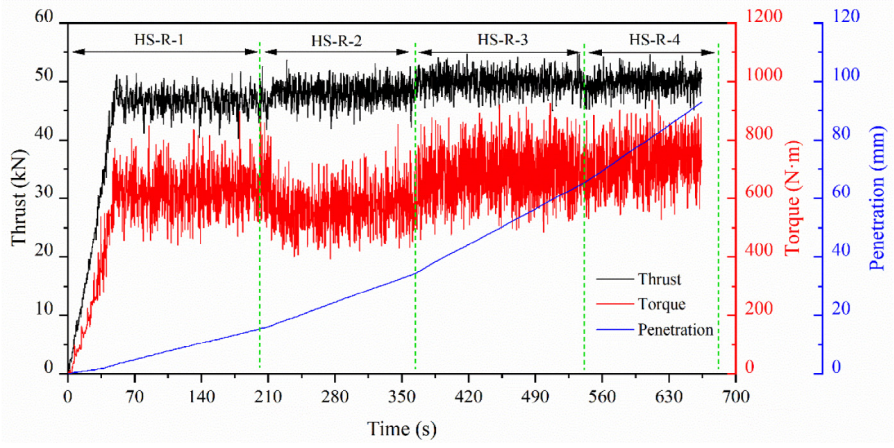

(c)

Fig. 8. Changes of tunnelling parameters under different rotational speeds during the test process using the three sandstone specimens. (a) Low-strength specimen, (b) medium-strength specimen, and (c) high-strength specimen.

hand, TBM tunnelling in low-strength specimens tends to break the rock by friction, resulting in small muck, while in medium-strength specimens, the rock is broken due to compression and shear, producing many flaky blocks of different sizes (Gong et al., 2021b; Wang et al., 2023). The strength increases again in high-strength specimens, and the disc cutter breaks the rock surface through friction. Thus, the trend of torque is similar to that obtained in a low-strength specimen. In addition, the box heights of the three rock specimens are close, indicating that the fluctuation range of the torque is similar under each scheme.

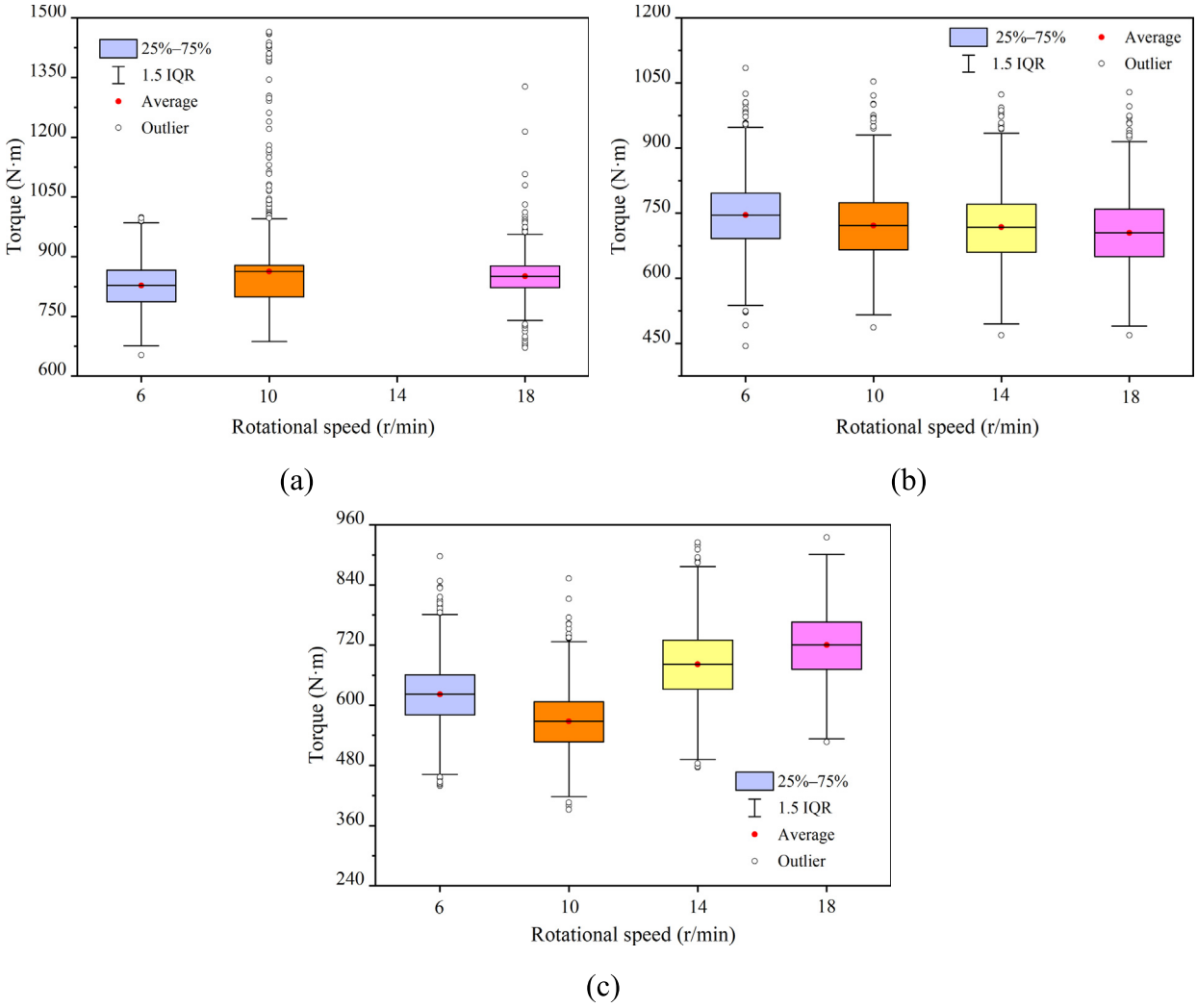

Fig. 9. Box plots of cutterhead torque under different rotational speeds using the three sandstone specimens. (a) Low-strength specimen, (b) medium-strength specimen, and (c) high-strength specimen.

Table 7
Averages of the TBM performance indices calculated from the stabilizing section in different rotational speeds.

Test No.	Variable (r/min)	T (N·m)	v (mm/min)	p_r (mm/r)	E_s (MJ/m^3)	I_{fp} (kN/mm·r)
LS-R-1	6	827.69	17.31	2.89	0.57	0.77
LS-R-2	10	832.10	25.49	2.55	0.57	0.87
LS-R-3	14	841.24	–	–	0.57	–
LS-R-4	18	848.77	49.89	2.77	0.57	0.80
MS-R-1	6	745.51	8.51	1.42	0.71	2.96
MS-R-2	10	721.56	12.77	1.28	0.71	2.46
MS-R-3	14	717.73	16.90	1.21	0.71	2.13
MS-R-4	18	704.77	20.25	1.13	0.71	1.99
HS-R-1	6	622.12	4.82	0.80	0.71	3.47
HS-R-2	10	568.16	7.13	0.71	0.71	3.91
HS-R-3	14	681.80	10.44	0.75	0.71	3.70
HS-R-4	18	720.09	13.44	0.75	0.71	3.70

3.2.2 Response law of TBM performance

The tunnelling parameters and performance indices (Table 7) are obtained from the stabling sections. The rotational speed effects on these parameters are analyzed, as shown in Fig. 10. As the rotational speed increases, the advance rate increases significantly, while the penetration

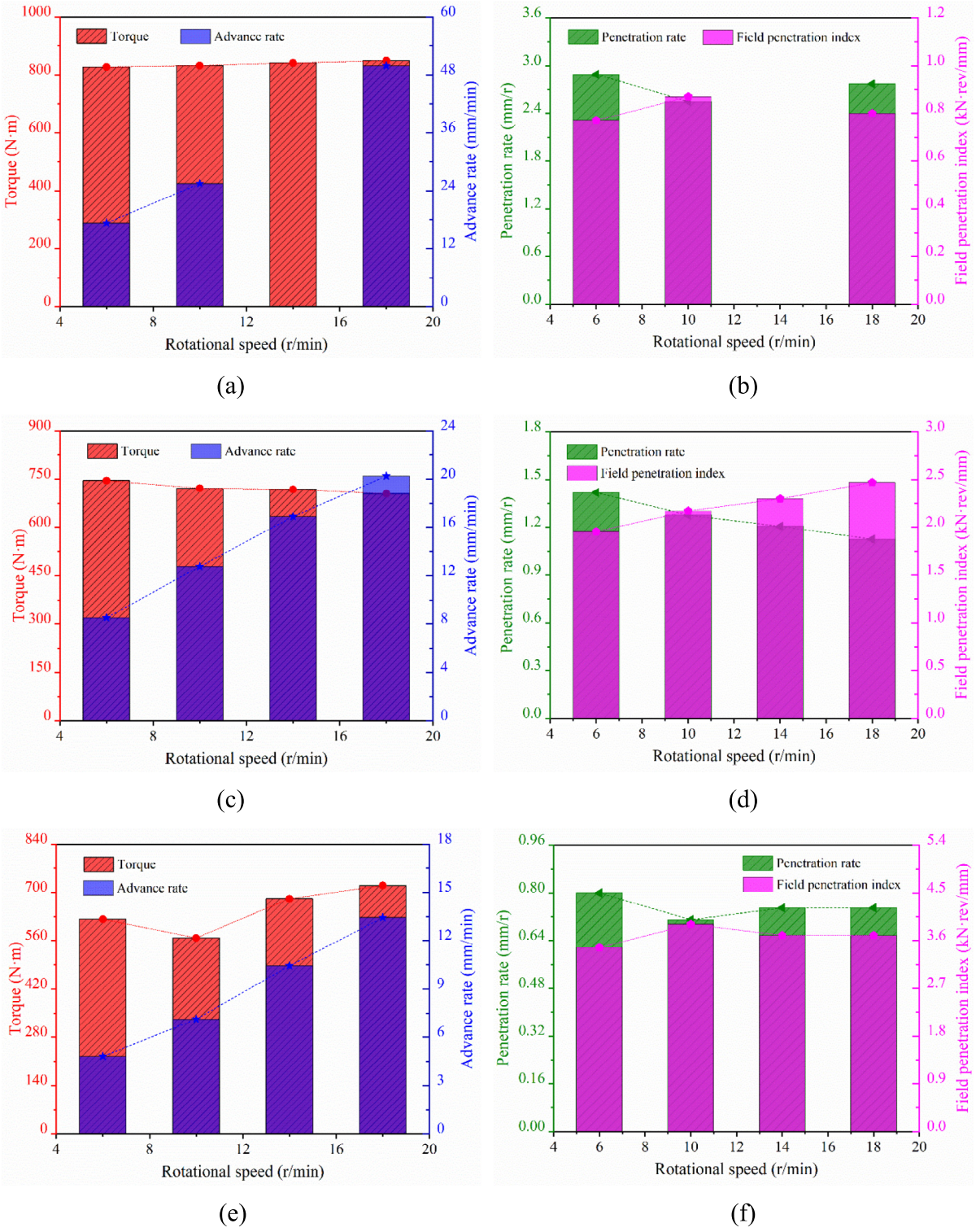

Fig. 10. Rotational speed effect on the torque and TBM performance indices using the three sandstone specimens with different strengths, including (a)–(b) low strength, (c)–(d) medium strength, and (e)–(f) high strength.

rate decreases slightly. The rotational speed shows different impacts on torque and field penetration index with the three sandstone specimens. In low- and high-strength specimens, the torque shows a slight increase. The field penetration index shows a trend of first increasing and then decreasing, while in the medium-strength specimen, the torque shows a slight decrease, and the field penetration index shows a trend of gradually increasing. Overall, the rota-

Table 8
Quantitative relationship models of the rotational speed effect on the torque and TBM performance indices.

Rock strength class	Index for TBM tunnelling	Model	R^2
Low strength	Torque	$T = 1.81n_{rpm} - 815.74$	0.983
	Advance rate	–	–
	Penetration rate	–	–
	Field penetration index	–	–
Medium strength	Torque	$T = -3.15n_{rpm} + 760.21$	0.916
	Advance rate	$v = 0.984n_{rpm} + 2.80$	0.997
	Penetration rate	$p_r = -0.02n_{rpm} + 1.54$	0.973
	Field penetration index	$I_{fp} = 5.73n_{rpm}^{-0.369}$	0.997
High strength	Torque	$T = 10.19n_{rpm} + 525.78$	0.620
	Advance rate	$v = 0.73n_{rpm} + 0.21$	0.995
	Penetration rate	$p_r = -0.003n_{rpm} + 0.79$	0.149
	Field penetration index	$I_{fp} = 3.275n_{rpm}^{-0.0498}$	0.212

tional speed effect on torque is not obvious, and the rotational speed is positively correlated with the field penetration index. The quantitative relationship models are established using the test results, as shown in Table 8. It shows that the tunnelling parameters and performance indices (except the PR and FPI in high-strength specimens) are highly correlated with the rotational speed. The correlations between the performance indices and rotational speed in low-strength specimens are not presented due to the data absence of $n_{rpm} = 14$ r/min.

3.2.3 Characteristics of rock muck

The rotational speed effect of the rock muck is discussed. As for the muck shape, the result is similar to that of the thrust effect (Fig. 6). The block is flatter when the size is larger, and more compact when the size is smaller. As for the muck size, the size distribution information under various schemes is statistically calculated, as shown in Table 9.

Figure 11 shows the rotational speed effect on the size distribution of rock muck. As the sieve size decreases, the residual mass on the sieve shows a trend of first increasing, then decreasing, and then increasing. The residual mass on the sieve with a size of 9.5 mm accounts for the smallest proportion, and that on the sieve with a size of 0.6 mm accounts for the largest proportion. In addition, as the rotational speed increases, the residual mass on the same-size sieve increases (the tunnelling time of the scheme with $n_{rpm} = 14$ r/min in a low-strength specimen is less than 150 s, resulting in insufficient rock muck collection). In terms of the muck CI, as the rotational speed increases, the CI of medium- and high-strength specimens shows a decreasing trend, while that of the low-strength specimen shows a slight increasing trend. Overall, as the rotational speed increases, the mass proportion of the muck powder increases. In this case, the TBM breaks the rock by friction, and the proportion of flat rock blocks decreases.

3.3 Rock strength effect on rock-cutterhead interaction

Three sandstone specimens with different strengths are used in the present study. This subsection discusses the strength effect on rock-cutterhead interaction in TBM tunnelling. The thrust and rotational speed should be kept as constants to eliminate their influences. There are two schemes with comparable strength among the 24 tunnelling test schemes (Table 3), namely, (1) $F = 50$ kN, $n_{rpm} = 6$ r/min; (2) $F = 40$ kN, $n_{rpm} = 10$ r/min. The box plots of the torque are shown in Fig. 12. The torque required for excavation in rock specimens with different strengths varies greatly. Under the condition (1), the torque required decreases as the rock strength increases. The box height (25%–75%) decreases, i.e., the fluctuation range of torque reduces. The trend of required torque in condition (2) is different. The required torque decreases first and then increases as the rock strength increases. The fluctuation range of torque in high-strength specimens shows a much wider range than that in low and medium-strength specimens. The potential reasons may be that the higher tunnelling vibration can be found when TBM drives in high strength specimen under high rotational speed. The opposite phenomenon can be found in low-strength specimens.

The rock strength effects on the TBM performance are presented in Fig. 13. As the rock strength increases, the torque, advance rate and penetration rate decrease, and the field penetration index increases. These indices can reflect the efficiency and cost in TBM tunnelling. Under the same tunnelling parameters, rocks with higher strength are more difficult to excavate (lower tunnelling efficiency). A smaller torque is required for rock breaking. The reason for the increase in the torque required for excavation in condition (2) is the wear of the cutter. The specific energy for the three sandstone specimens is constant (Tables 4 and 7).

Figure 14 shows the influence of rock strength on the muck produced from the TBM tunnelling test. As the rock strength increases, the residual mass of muck

Table 9
Muck information obtained from tunnelling tests with different rotational speeds and rock specimens.

Test No.	Mass and mass percent of rock muck remaining in the sieve meshes with different diameters (mm)										CI
	$d_s > 9.5$		$4.75 < d_s \leq 9.50$		$2.36 < d_s \leq 4.75$		$1.18 < d_s \leq 2.36$		$0.60 < d_s \leq 1.18$		$d_s \leq 0.60$		
	Weight (kg)	Percent (%)	Weight (kg)	Percent (%)	Weight (kg)	Percent (%)	Weight (kg)	Percent (%)	Weight (kg)	Percent (%)	Weight (kg)	Percent (%)	
LS-R-1	0.05	1.07	0.78	16.74	0.60	12.88	0.24	5.15	0.15	3.22	2.84	60.94	224.46
LS-R-2	0.05	0.83	1.11	18.53	0.74	12.35	0.33	5.51	0.20	3.34	3.56	59.43	229.72
LS-R-3	0.02	0.80	0.47	18.73	0.35	13.94	0.14	5.58	0.09	3.59	1.44	57.37	235.46
LS-R-4	0.03	0.43	1.17	16.96	0.89	12.90	0.36	5.22	0.23	3.33	4.22	61.16	222.46
MS-R-1	0.02	0.88	0.31	13.6	0.36	15.79	0.27	11.84	0.28	12.28	1.04	45.61	242.11
MS-R-2	0.01	0.24	0.61	14.39	0.65	15.33	0.49	11.56	0.53	12.5	1.95	45.99	240.33
MS-R-3	0.00	0.00	0.54	9.94	0.80	14.73	0.65	11.97	0.74	13.63	2.70	49.72	221.55
MS-R-4	0.00	0.00	0.65	8.75	1.15	15.48	0.96	12.92	1.03	13.86	3.64	48.99	221.13
HS-R-1	0.07	2.88	0.7	28.81	0.48	19.75	0.24	9.88	0.15	6.17	0.79	32.51	314.81
HS-R-2	0.11	3.45	1.04	32.60	0.57	17.87	0.29	9.09	0.18	5.64	1.00	31.35	325.08
HS-R-3	0.11	2.04	1.43	26.48	1.04	19.26	0.56	10.37	0.35	6.48	1.91	35.37	301.11
HS-R-4	0.11	1.75	1.65	26.19	1.15	18.25	0.65	10.32	0.41	6.51	2.33	36.98	295.40

remaining on the sieve with the same size decreases, and the coarseness index increases. Namely, less powder proportion is produced from the tunnelling in specimens with higher strength. In this case, the rock breaking is more effective to produce flat blocks of a larger size. To further establish the rock-cutterhead interaction relationships, the rock mechanical properties in Table 2 are used to correlate with the coarseness index. These correlations have high coefficients of determination. The slopes of the correlations in condition (1) marked in black are close to those of the corresponding correlations in condition (2) marked in red. Thus, these correlations can be used to evaluate the rock properties or TBM performance in TBM tunnelling.

Figure 15 shows the three sandstone specimens after tunnelling tests, conducted with an excavation diameter of 300 mm. A series of concentric trajectories can be seen in the tunnel face. The low specimen is broken during the lifting process after the test. Two expansion bolts are installed on the upper plane to support lifting. Notably, some of the produced muck exceeds the largest sieve size (9.5 mm) used in this study. This occurs because, at the initial rock-cutter contact, a completely free plane exists, allowing large muck to form when cracks propagate to the free surface. Consequently, such muck, originating from the free plane, is excluded from the size distribution analysis. Additionally, a boundary curve larger than the excavation line is observable on the rock specimen's surface.

The current study employs rock specimens of a specific type and strength to investigate the rock-cutterhead interaction. Certain limitations should be noted: the sandstone specimens were not subjected to confining pressure to simulate in-situ geostress. To enhance the platform's applicability, additional experiments should explore varying rock conditions (e.g., rock type, strength, joint distribution, and confining pressure) and TBM operational parameters (e.g., tunnelling settings, cutterhead design, and control modes). Thus, further research is urgently required to refine the understanding of rock-machine interactions and validate the functionalities of the proposed DGTBM-A platform.

3.4 Validation of tunnelling testing results

As illustrated in Fig. 16 (a), a disc cutter is subjected to three orthogonal forces during rock or rock mass cutting (Rostami, 1997): the normal force F_n perpendicular to the rock surface, the rolling force F_r along the cutter's rotational direction, and the side force F_s perpendicular to the cutter's rotation plane. These forces correlate with TBM tunnelling response parameters as follows: F_n contributes the thrust, F_r contributes the torque, and F_s has little influence on the tunnelling parameters (Cho et al., 2010; Heydari et al., 2019). Currently, the rock-breaking mechanisms of disc cutter primarily include the compression-breaking model, compression-shear breaking model, and

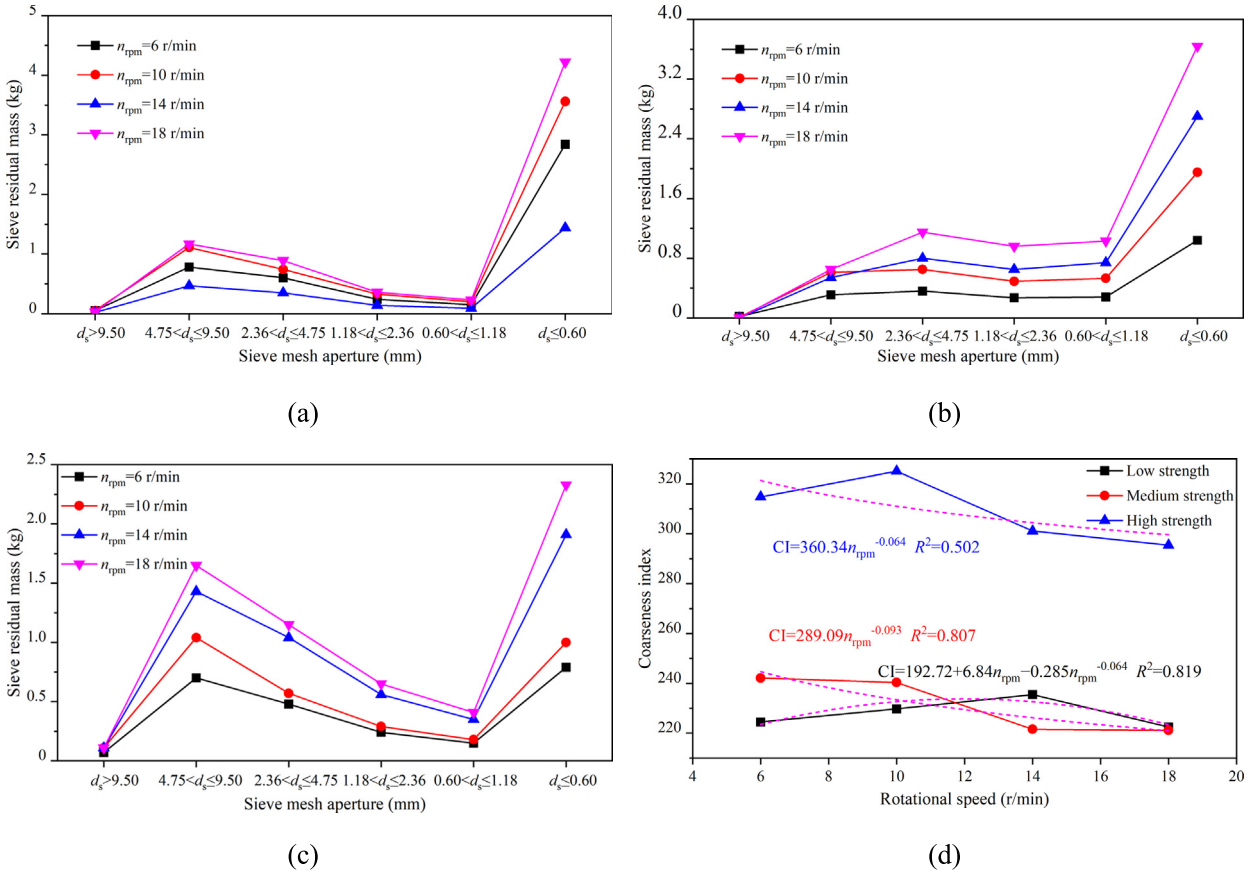

Fig. 11. Muck information collected from the tunnelling tests with different rotational speeds and sandstone specimens. (a) Low-strength specimen, (b) medium-strength specimen, (c) high-strength specimen, and (d) relationships between coarseness index and rotational speed.

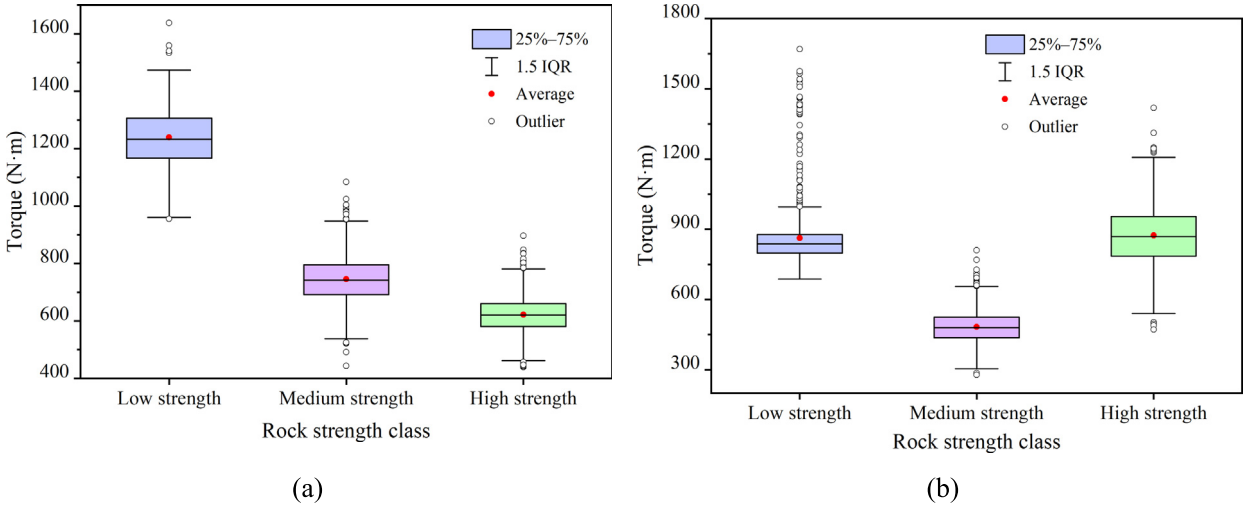

Fig. 12. Box plots of rock strength effect on cutterhead torque with the same tunnelling parameters. (a) $F = 50$ kN, $n_{rpm} = 6$ r/min, and (b) $F = 40$ kN, $n_{rpm} = 10$ r/min.

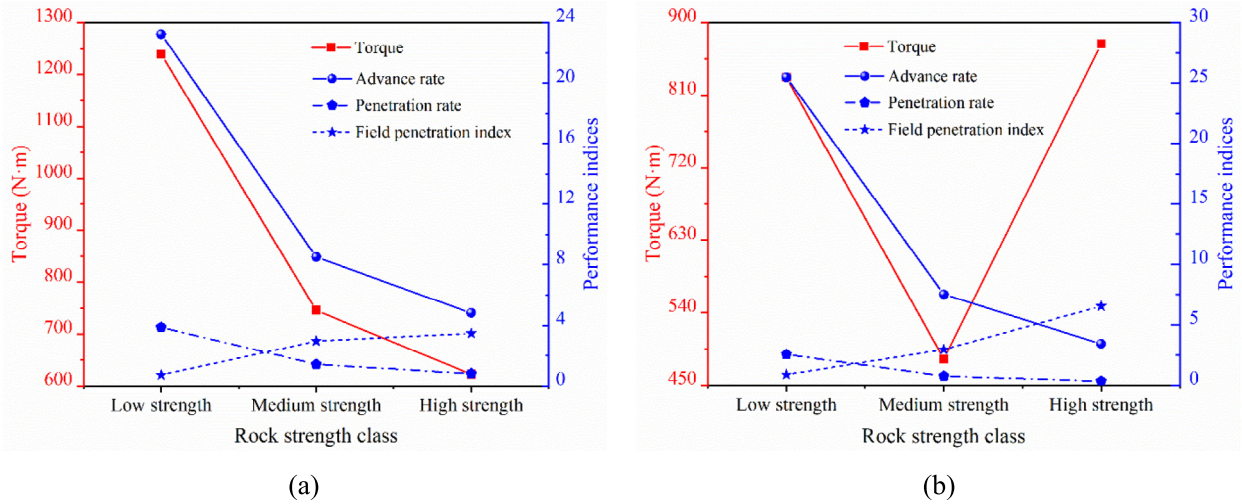

Fig. 13. Rock strength effect on the torque and TBM performance indices. (a) $F = 50$ kN, $n_{rpm} = 6$ r/min, and (b) $F = 40$ kN, $n_{rpm} = 10$ r/min.

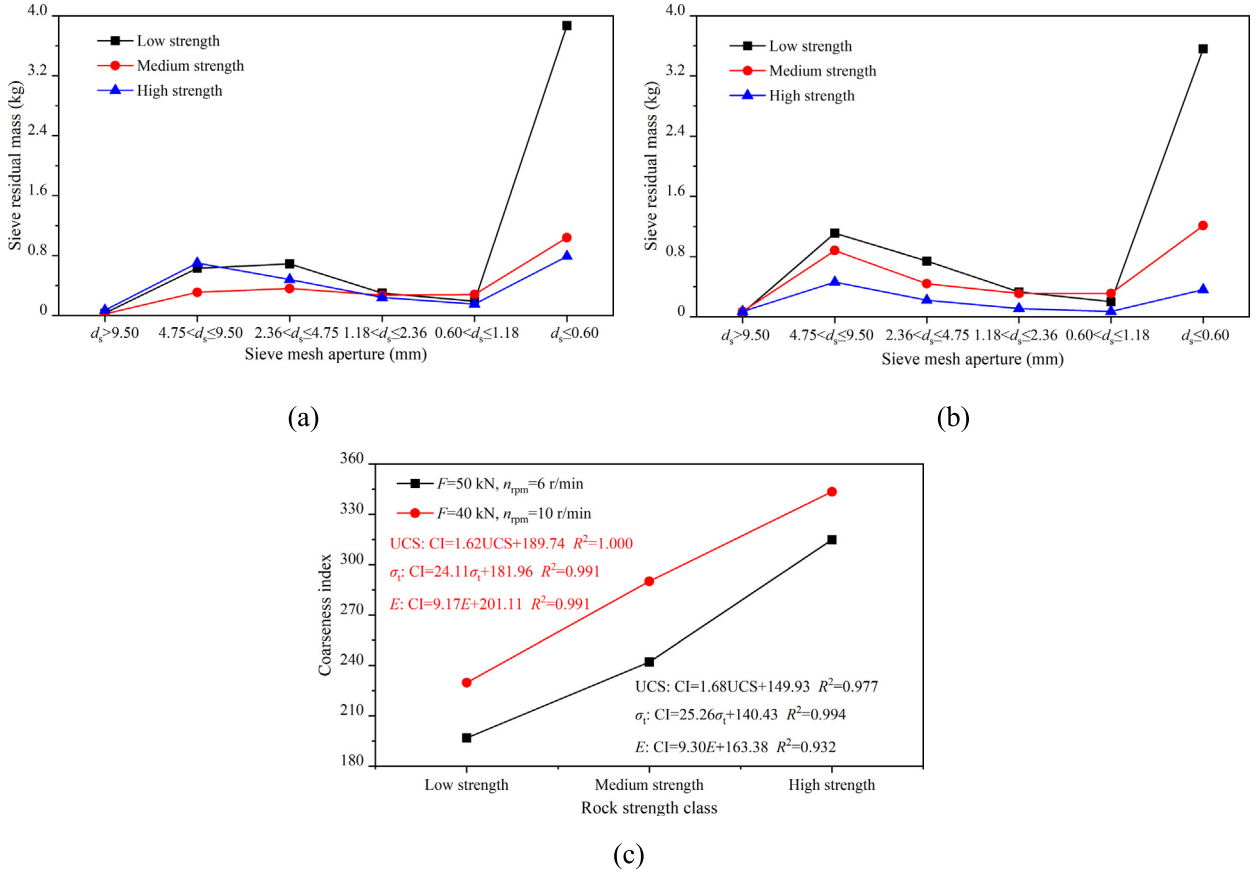

Fig. 14. Rock strength effect on the rock muck mass and coarseness index. (a) $F = 50$ kN, $n_{rpm} = 6$ r/min, (b) $F = 40$ kN, $n_{rpm} = 10$ r/min, and (c) relationships between coarseness index and rock strength class.

compression-tension breaking model (Innaurato & Oreste, 2011; Xie et al., 2024), as depicted in Fig. 16(b)–(d).

Compression-breaking model. Rock failure occurs when the normal force exceeds the rock's uniaxial compressive strength.

Compression-shear breaking model. Rock is fractured through combined compressive and shear forces. Under normal force, a dense core forms beneath the cutter, while shear forces crush the surrounding rock, creating a near-triangular fracture zone (Xie et al., 2024).

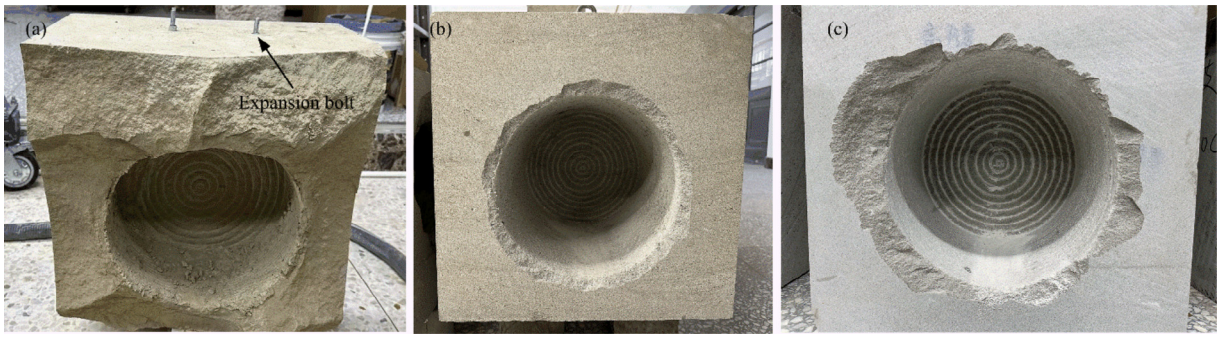

Fig. 15. Three sandstone specimens after tunnelling tests. (a) Low-strength specimen, (b) medium-strength specimen, and (c) high-strength specimen.

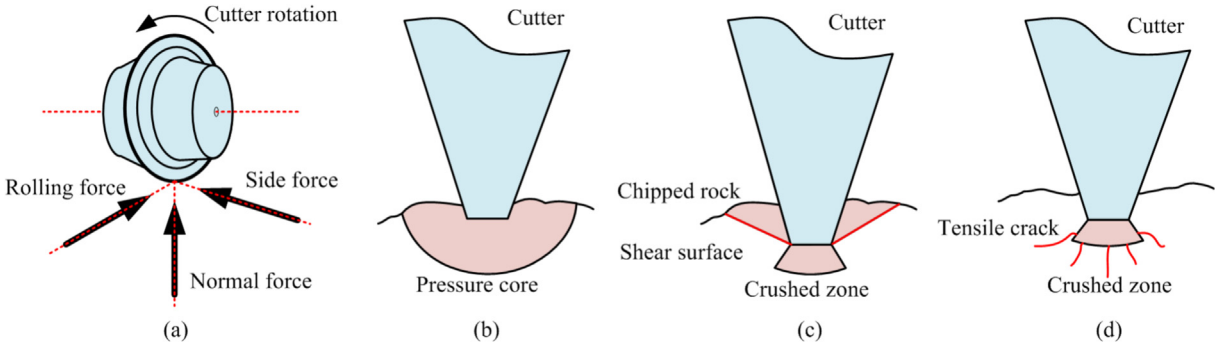

Fig. 16. Schematic diagram of cutting force in rock-machine interaction and the rock breaking mechanisms. (a) Rock cutting forces, modified from Rostami (1997), (b) compression breaking model, (c) compression-shear breaking model, and (d) compression-tension breaking model, modified from Tian (2021).

Table 10
Theoretical models calculating the cutting forces of the TBM cutter.

Reference	Normal force F_n	Normal force F_r
Evans model (Evans & Pomery, 1966)	$F_n = 4/3\sigma_c p\sqrt{\left[R^2-(R-p)^2\right]}\tan(\theta/2)$	–
Roxborough model (Roxborough & Phillops, 1975)	$F_n = 4\sigma_c\sqrt{\left[Rp^3-p^4\right]}\tan(\theta/2)$	$F_r = 4\sigma_c p^2\tan(\theta/2)$
Wijk model (Wijk, 1992)	$F_n = 3\sigma_c[w+p\tan(\theta/2)]\sqrt{Dp}$	$F_r = \sigma_c p[3w+2p\tan(\theta/2)]$
SJTU model (Sun et al., 1980)	$F_n = kr\frac{E_1+E_2}{E_1E_2}\sqrt{Dh}\sigma_c^2$	$F_r = F_n\left(\sqrt{\frac{p}{D}}+\mu\frac{d}{D}\right)$
CSM model (Rostami, 1997)	$F_n = D^{0.5}p^{1.5}[4/3\sigma_c+2\tau(s/p-2\tan(\theta/2))]\tan(\theta/2)$	$F_r = \left[\sigma_c p^2+\frac{4\tau\phi(s-2p\tan(\theta/2))}{D(\phi\text{-}\sin\phi\cos\phi)}\right]\tan(\theta/2)$
Sanio model (Sanio, 1985)	$F_n = 3/25\sqrt{I_{s(50)}Dsp}\cdot\tan(\theta/2)$	$F_r = 4/5(p/D)^{0.5}F_n$
NEU model (Xu & Yu, 1984)	$F_n = 4/3k_d\sigma_c p\sqrt{R^2-(R-p)^2}\tan(\varphi/2)$	$F_r = \varepsilon k_d\sigma_c p^2\tan(\varphi/2)$

Compression-tension breaking model. Rock failure results from combined compression and tensile stresses. Tensile forces induce crack propagation, and when adjacent cracks coalesce, rock fragmentation occurs.

A series of models has been proposed using the theoretical mechanisms to calculate the cutting forces of the disc cutter (Table 10). Since the side force has a negligible influence on the cutterhead, it is typically excluded from calculations. The F_n and F_r of the single cutter can be calculated using these equations. Then the thrust and torque of the cutterhead can be obtained according to Eqs. (6) and (7) (Rostami, 1997):

$$F = NF_n, \tag{6}$$

$$T = \sum_{i=1}^{n} F_{ri}\rho_i \approx 0.3ND_cF_r, \tag{7}$$

Table 11
Calculation parameters for the theoretical models.

Symbol	Definition	Value
R	Cutter radius (mm)	25
p	Penetration (mm)	Refer to p_r in Tables 4 and 7
σ_c	Uniaxial strength of rock (MPa)	Refer to UCS in Table 2
θ	Cutter edge angle (°)	121
s	Cutter spacing (mm)	15
τ	Shear strength (MPa)	About $1/10\sigma_c$
ϕ	Disk cutter angle of rock catching (°)	$\phi = \arccos((R-p)/R)$
D	Cutter diameter (mm)	50
w	Blade width of disc cutter (mm)	4
k_d	Rolling conversion factor	0.45 for specimen #1, 0.55 for specimen #2, and 0.65 for specimen #3
φ	Rock body crushing angle (°)	145
ε	Conversion factor	2.25
r	Tip radius of the rounded corner of the cutter (mm)	2
E_1	Elastic modulus of the cutter (MPa)	217 000
E_2	Elastic modulus of the rock (MPa)	Refer to E in Table 2
k	Coefficient	$k = 2600$
μ	Equivalent friction coefficient of supporting rolling bearings, friction of cutting edge, etc.	$\mu = 0.02$
d	Diameter of cutter shaft (mm)	20
$I_{s(50)}$	Point load strength	$I_{s(50)} = \left(\frac{\sigma_c}{22.82}\right)^{4/3}$
σ_t	Rock tensile strength	Refer to σ_t in Table 2

where F and T are the thrust and torque of the cutterhead, respectively. N is the number of disc cutters. F_n is the normal force. F_r is the rolling force. F_{ri} is the rolling force of the ith disc cutter at the mounting radius ρ_i. D_c is the cutterhead diameter.

The parameters for the calculations of the cutting forces in the theoretical models above are summarized in Table 11. These parameters are determined from the commonly used rock specimens in the references and the mechanical properties of sandstone specimens in this study.

The comparison of theoretical models and experimental results for thrust (Fig. 17(a)) shows that the experimental data align closely with several established theories, such as CSM Evans, and Roxborough models. Evans model shows good estimation of thrust in low-strength specimen (specimen #1), while Roxborough model shows good estimation of thrust in medium-strength specimen (specimen #2). The thrust provided by the remaining four models differs significantly from the experimental results. These models may need to be revised for the rock-machine interaction, especially for the high-strength rock under cutting conditions. The consistency across multiple studies (CSM model) further validates the reliability of the experimental approach in this work. For torque (Fig. 17(b)), the experimental results exhibit a clear distinction between low-, medium-, and high-strength specimens, with the theoretical (CSM) model providing reasonable prediction for these specimens. The remaining models overestimate or underestimate the torque seriously. The required torque decreases as the rock strength increases, and this conclusion is consistent with the experimental results in Fig. 12(a). Generally, the CSM model provides the best estimation of thrust and torque when TBM drives in rock with different strengths.

4 Conclusions

The present study proposed a novel TBM tunnelling test platform. The platform is composed of a tunnelling subsystem, a hydraulic loading subsystem, a sample installation subsystem, a control subsystem, and an integrated monitoring subsystem. The response law of rock-cutterhead interaction in intact sandstone specimens is studied using the platform, including thrust effect, rotational speed effect and rock strength effect. The following conclusions can be drawn:

(1) As the thrust increases, the torque, advance rate, and specific energy increase, and the field penetration index decreases. The mass of rock muck remaining on the sieve with the same size increases, the coarseness index decreases, and more powder in the rock muck is produced in TBM tunnelling.
(2) As the rotational speed increases, the advance rate increases significantly, the penetration rate decreases slightly, and no obvious impact is found on the torque. More muck with a smaller size is produced. In addition, the TBM cutter tends to break the rock by friction, and the proportion of flat rock blocks decreases.
(3) As the rock strength increases, the torque, advance rate, and penetration rate decrease, and the field penetration index increases. The mass of rock muck remaining on the sieve with the same size decreases, and the coarseness index increases. Thus, the powder mass produced by TBM excavation in higher-strength rocks accounts for a smaller proportion.
(4) The shape of muck with a large size tends to be flat, and small muck tends to be compact in shape. In addition, as the sieve size decreases, the residual mass

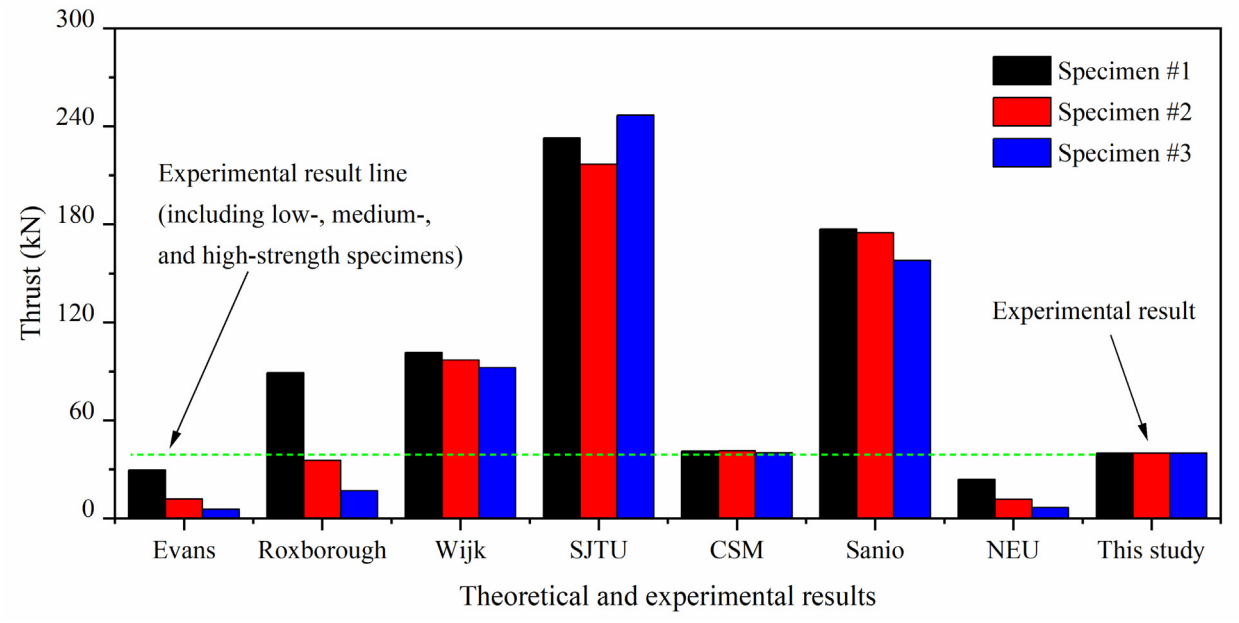

(a)

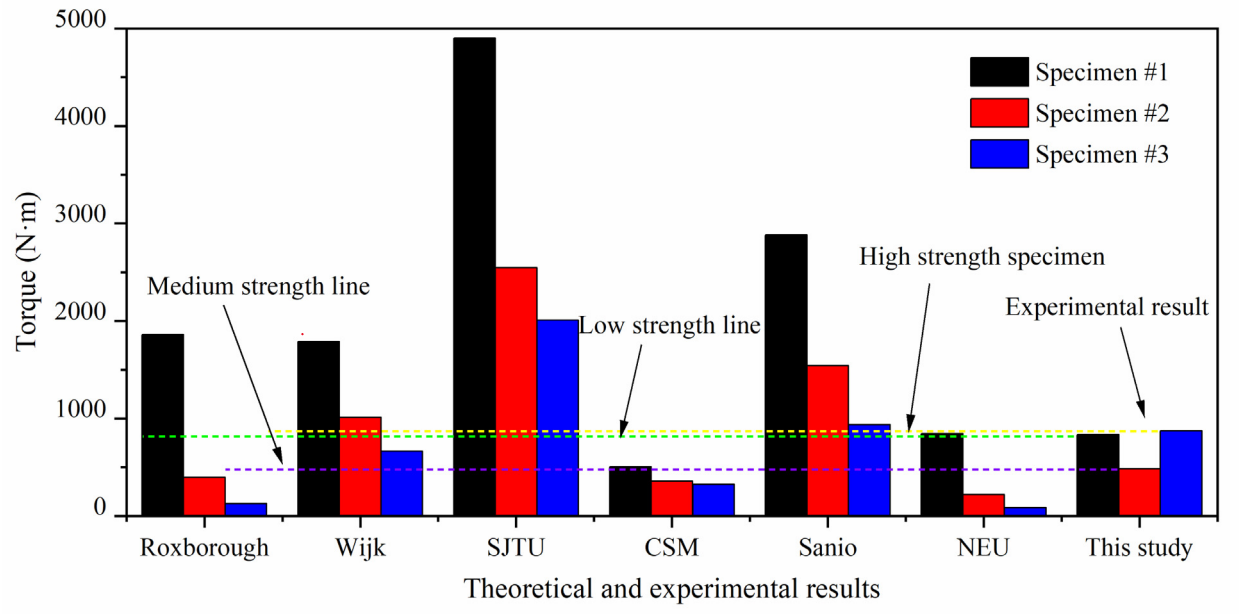

(b)

Fig. 17. Comparisons between the theoretical analysis and experimental study. (a) Thrust, and (b) torque.

on the sieve shows a trend of first increasing, then decreasing, and then increasing. The residual mass on the largest sieve accounts for the smallest proportion, and the residual mass of the powder accounts for the largest proportion. The above tunnelling test results are consistent with the TBM tunnelling in engineering practice, indicating the feasibility and effectiveness of the novel TBM tunnelling test platform proposed in this study.

Data availability

The data that support the findings of this study are available from the corresponding author upon reasonable request.

CRediT authorship contribution statement

Weiqiang Xie: Methodology, Writing – original draft, Conceptualization, Funding acquisition. **Xiaoli Liu:** Project

administration, Supervision, Writing – review & editing, Funding acquisition. **Caifeng Zhang:** Validation, Investigation, Resources. **Xiaoxiong Zhou:** . **Jian Chen:** Visualization, Software, Validation.

Declaration of competing interest

The authors declare that they have no known competing financial interests or personal relationships that could have appeared to influence the work reported in this paper.

Acknowledgement

The authors would like to thank the Yunlong Lake Laboratory of Deep Underground Science and Engineering (Grant No. 104023005), the National Natural Science Foundation of China (Grant No. 52308403), and the State Key Laboratory of Hydroscience and Engineering (Grant Nos. sklhse-TD-2024-D02 and sklhse-2024-D-04) for funding provided to this work.

References

Armaghani, D. J., Liu, Z., Khabbaz, H., Fattahi, H., Li, D., & Afrazi, M. (2024). Tree-based solution frameworks for predicting tunnel boring machine performance using rock mass and material properties. *Computer Modeling in Engineering and Sciences, 141*(3), 2421–2451.

Bakar, M. Z. A., Gertsch, L. S., & Rostami, J. (2014). Evaluation of fragments from disc cutting of dry and saturated sandstone. *Rock Mechanics and Rock Engineering, 47*(5), 1891–1903.

Barton, N. (2000). *TBM tunnelling in jointed and faulted rock*. Rotterdam, Brookfield: AA Balkema.

Bejari, H. (2013). Simultaneous effects of joint spacing and orientation on TBM cutting efficiency in jointed rock masses. *Rock Mechanics and Rock Engineering, 46*(4), 897–907.

Chen, Z., Zhang, Y., Li, J., Xu, L., & Jing, L. (2020). Diagnosing tunnel collapse sections based on TBM tunneling big data and deep learning: A case study on the Yinsong Project. *China. Tunnelling and Underground Space Technology, 108*, 103700.

Cho, J. W., Jeon, S., Yu, S. H., & Chang, S. H. (2010). Optimum spacing of TBM disc cutters: A numerical simulation using the three-dimensional dynamic fracturing method. *Tunnelling and Underground Space Technology, 25*(3), 230–244.

Delisio, A., Zhao, J., & Einstein, H. H. (2013). Analysis and prediction of TBM performance in blocky rock conditions at the Loetschberg Base Tunnel. *Tunnelling and Underground Space Technology, 33*, 131–142.

Evans, I., & Pomery, C. D. (1966). *The strength fracture and workability of coal*. London: Pergamon Process.

Feng, S., Chen, Z., Luo, H., Wang, S., Zhao, Y., Liu, L., Ling, D., & Jing, L. (2021). Tunnel boring machines (TBM) performance prediction: A case study using big data and deep learning. *Tunnelling and Underground Space Technology, 110*, 103636.

Feng, X.-T., Su, X.-X., Yang, C.-X., Lin, F., Li, S.-P., Zhang, J.-Y., & Tong, T.-Y. (2024). A test system for microwave-assisted dual-mode mechanical cutting of hard rock under true triaxial compression. *Rock Mechanics and Rock Engineering, 57*(8), 5763–5782.

Fu, K., Qiu, D., Xue, Y., Tao, Y., & Kong, F. (2024). Research on optimization strategy of TBM tunneling parameters based on stratum perception and simulation tunneling experiment. *Tunnelling and Underground Space Technology, 147*, 105743.

Geng, Q., Zhang, H., Liu, X., & Wang, X. (2019). Numerical study on the rock muck transfer process of TBM cutterhead with clump strategy based on discrete element method. *Tunnelling and Underground Space Technology incorporating Trenchless Technology Research, 91*, 103000.

Gong, Q., Liu, Q., & Zhang, Q. (2016). Tunnel boring machines (TBMs) in difficult grounds. *Tunnelling and Underground Space Technology, 57*, 1–3.

Gong, Q., Lu, J., Xu, H., Chen, Z., Zhou, X., & Han, B. (2021a). A modified rock mass classification system for TBM tunnels and tunneling based on the HC method of China. *International Journal of Rock Mechanics and Mining Sciences, 137*, 104511.

Gong, Q., Xu, H., Lu, J., Wu, F., Zhou, X., & Yin, L. (2022). Rock mass characteristics model for TBM penetration rate prediction– an updated version. *International Journal of Rock Mechanics and Mining Sciences, 149*, 104993.

Gong, Q., Zhou, X., Liu, Y., Bei, H., & Yin, L. (2021b). Development of a real-time muck analysis system for assistant intelligence TBM tunnelling. *Tunnelling and Underground Space Technology, 107*, 103655.

Gong, Q. M., Zhao, J., & Jiang, Y. S. (2007). In situ TBM penetration tests and rock mass boreability analysis in hard rock tunnels. *Tunnelling and Underground Space Technology, 22*(3), 303–316.

Goodarzi, S., Hassanpour, J., Yagiz, S., & Rostami, J. (2021). Predicting TBM performance in soft sedimentary rocks, case study of Zagros mountains water tunnel projects. *Tunnelling and Underground Space Technology, 109*, 103705.

Hassanpour, J., Firouzei, Y., & Hajipour, G. (2020). Actual performance analysis of a double shield TBM through sedimentary and low to medium grade metamorphic rocks of Ghomrood water conveyance tunnel project (lots 3 and 4). *Bulletin of Engineering Geology and the Environment, 80*(2), 1419–1432.

Hassanpour, J., Rostami, J., Khamehchiyan, M., & Bruland, A. (2009). Developing new equations for TBM performance prediction in carbonate-argillaceous rocks: A case history of Nowsood water conveyance tunnel. *Geomechanics and Geoengineering, 4*(3), 287–297.

Hassanpour, J., Rostami, J., Zhao, J., & Azali, S. T. (2015). TBM performance and disc cutter wear prediction based on ten years experience of TBM tunnelling in Iran. *Geomechanik Und Tunnelbau, 8*(3), 239–247.

Heydari, S., Hamidi, J. K., Monjezi, M., & Eftekhari, A. (2019). An investigation of the relationship between muck geometry, TBM performance, and operational parameters: A case study in Golab II water transfer tunnel. *Tunnelling and Underground Space Technology, 88*, 73–86.

Hou, S., Liu, Y., & Yang, Q. (2022). Real-time prediction of rock mass classification based on TBM operation big data and stacking technique of ensemble learning. *Journal of Rock Mechanics and Geotechnical Engineering, 14*(1), 123–143.

Innaurato, N., & Oreste, P. (2011). Theoretical study on the TBM tool-rock interaction. *Geotechnical and Geological Engineering, 29*, 297–305.

Jeong, H., & Jeon, S. (2018). Characteristic of size distribution rock chip produced by rock cutting with a pick cutter. *Geomechanics and Engineering, 15*, 811–822.

Jing, L. J., Li, J. B., Zhang, N., Chen, S., Yang, C., & Cao, H. B. (2021). A TBM advance rate prediction method considering the effects of operating factors. *Tunnelling and Underground Space Technology, 107*, 103620.

Khetwal, A., Rostami, J., & Nelson, P. P. (2020). Investigating the impact of TBM downtimes on utilization factor based on sensitivity analysis. *Tunnelling and Underground Space Technology, 106*, 103586.

Lee, G.-J., & Kwon, T.-H. (2023). Discharge behavior of spherical and rock chip mucks by screw conveyors in TBM: Physical model experiments and DEM simulations. *Tunnelling and Underground Space Technology, 142*, 105407.

Li, J. B., Chen, Z. Y., Li, X., Jing, L. J., Zhang, Y. P., Xiao, H. H., Wang, S. J., Yang, W. K., Wu, L. J., Li, P. Y., Li, H. B., Yao, M., & Fan, L. T. (2023a). Feedback on a shared big dataset for intelligent TBM Part II: Application and forward look. *Underground Space, 11*, 26–45.

Li, J. B., Chen, Z. Y., Li, X., Jing, L. J., Zhangf, Y. P., Xiao, H. H., Wang, S. J., Yang, W. K., Wu, L. J., Li, P. Y., Li, H. B., Yao, M., & Fan, L. T. (2023b). Feedback on a shared big dataset for intelligent TBM Part I: Feature extraction and machine learning methods. *Underground Space, 11*, 1–25.

Liu, Q., Liu, J., Pan, Y., Kong, X., & Hong, K. (2017). A case study of TBM performance prediction using a Chinese rock mass classification system – Hydropower Classification (HC) method. *Tunnelling and Underground Space Technology, 65*, 140–154.

Ma, H., Wang, J., Man, K., Chen, L., Gong, Q., & Zhao, X. (2020). Excavation of underground research laboratory ramp in granite using tunnel boring machine: Feasibility study. *Journal of Rock Mechanics and Geotechnical Engineering, 12*, 1201–1213.

Mostafa, S., Sousa, R. L., & Einstein, H. H. (2024). Toward the automation of mechanized tunneling "exploring the use of big data

analytics for ground forecast in TBM tunnels". *Tunnelling and Underground Space Technology, 146*, 105643.
Nouri, M., Khanlari, G., Rafiei, B., Sarfarazi, V., & Zaheri, M. (2022). Estimation of brittleness indexes from petrographic characteristics of different sandstone types (cenozoic and mesozoic sandstones), Markazi Province. *Iran. Rock Mechanics and Rock Engineering, 55*(4), 1955–1995.
Pan, Y., Fu, X., & Zhang, L. (2022). Data-driven multi-output prediction for TBM performance during tunnel excavation: An attention-based graph convolutional network approach. *Automation in Construction, 141*, 104386.
Rostami, J. (1997). Development of a force estimation model for rock fragmentation with disc cutters through theoretical modeling and physical measurement of crushed zone pressure. [Doctoral dissertation, Colorado School of Mines].
Rostami, J. (2016). Performance prediction of hard rock Tunnel Boring Machines (TBMs) in difficult ground. *Tunnelling and Underground Space Technology, 57*, 173–182.
Roxborough, F. F., & Phillops, H. R. (1975). Rock excavation by disc cutter. *International Journal of Rock Mechanics and Mining Sciences and Geomechanics Abstracts, 12*(12), 361–366.
Salimi, A., Rostami, J., & Moormann, C. (2019). Application of rock mass classification systems for performance estimation of rock TBMs using regression tree and artificial intelligence algorithms. *Tunnelling and Underground Space Technology, 92*, 103046.
Sanio, H. P. (1985). Prediction of the performance of disc cutters in anisotropic rock. *International Journal of Rock Mechanics and Mining Science and Geomechanics Abstracts, 22*(3), 153–161.
Sun, H. F., Chen, J. Y., & Chen, G. (1980). Research on rock breaking force and calculated load of TBM cutters. *Construction Machinery and Equipment, 8*, 1–7 (in Chinese).
Tan, Q., Yi, L., & Xia, Y. M. (2018). Performance prediction of TBM disc cutting on marble rock under different load cases. *KSCE Journal of Civil Engineering, 22*(4), 1466–1472.
Tang, S., Zhang, X., Liu, Q., Zhang, Q., Li, X., & Wang, H. (2024). Experimental study on the influences of cutter geometry and material on scraper wear during shield TBM tunnelling in abrasive sandy ground. *Journal of Rock Mechanics and Geotechnical Engineering, 16*, 410–425.
Tian, J. (2021). *Study on wear mechanism and rock breaking characteristics of TBM disc cutters*. Jilin, China: Jilin University (in Chinese).
Tuncdemir, H., Bilgin, N., Copur, H., & Balci, C. (2008). Control of rock cutting efficiency by muck size. *International Journal of Rock Mechanics and Mining Sciences, 45*(2), 278–288.
Ulusay, R. (2015). *The ISRM suggested methods for rock characterization, testing and monitoring, 2007–2014*. Cham: Springer International Publishing.
Wang, J., Zhang, Y., Wang, K., Li, L., Cheng, S., & Sun, S. (2024a). Development of similar materials with different tension-compression ratios and evaluation of TBM excavation. *Bulletin of Engineering Geology and the Environment, 83*(5), 190.
Wang, P., Yue, Z., Li, A., Ren, M., Gao, D., & Bu, W. (2023). Experimental and analytical study on key factors of rock breaking under a single indenter. *Fatigue & Fracture of Engineering Materials & Structures, 46*(5), 1997–2016.
Wang, X., Li, S., Yuan, C., Ma, P., Han, Y., & Peng, K. (2024b). Experimental study on the wear and temperature of TBM disc cutter under different tunneling parameters. *Tunnelling and Underground Space Technology, 149*, 105789.
Wijk, G. (1992). A model of tunnel boring machine performance. *Geotechnical and Geological Engineering, 10*(1), 19–40.
Wu, Z., Wei, R., Chu, Z., & Liu, Q. (2021). Real-time rock mass condition prediction with TBM tunneling big data using a novel rock–machine mutual feedback perception method. *Journal of Rock Mechanics and Geotechnical Engineering, 13*(6), 1311–1325.
Wu, Z., Zhang, P., Fan, L., & Liu, Q. (2019). Numerical study of the effect of confining pressure on the rock breakage efficiency and fragment size distribution of a TBM cutter using a coupled FEM-DEM method. *Tunnelling and Underground Space Technology, 88*, 260–275.
Xie, W. Q., Zhang, X. P., Liu, Q. S., Tang, S. H., & Li, W. W. (2021). Experimental investigation of rock strength using indentation test and point load test. *International Journal of Rock Mechanics and Mining Sciences, 139*, 104647.
Xie, W. Q., Zhang, X. P., Liu, X. L., Xu, C. Y., Li, X. F., Song, D. Q., Ma, Q., & Hu, N. (2023). Real-time perception of rock–machine interaction information in TBM tunnelling using muck image analysis. *Tunnelling and Underground Space Technology, 136*, 105096.
Xie, W. Q., Liu, X. L., Qian, R. P., Chen, J., Wang, E. Z., & Hong, W. (2025). Development of a novel TBM tunnelling test platform and its application in rock–machine interaction analysis. *Rock Mechanics and Rock Engineering, 58*(1), 867–885.
Xie, W. Q., Liu, X. L., Zhang, X. P., Yang, X. M., & Zhou, X. X. (2024). A critical review of rock indentation: Theories, experiments, numerical simulations, and applications. *Journal of Rock Mechanics and Geotechnical Engineering, 16*(6), 2351–2374.
Xu, X. H., & Yu, J. (1984). *Rock fragmentation*. Beijing: Coal Industry Press, in Chinese.
Xu, H., Gong, Q., Zhou, X., Yang, F., & Han, B. (2024). Vibration analysis of rock breaking by TBM rolling cutter assisted with various depth kerfs. *Tunnelling and Underground Space Technology, 146*, 105634.
Yagiz, S. (2008). Utilizing rock mass properties for predicting TBM performance in hard rock condition. *Tunnelling and Underground Space Technology Incorporating Trenchless Technology Research, 23*(3), 326–339.
Yu, S., Zhang, Z., Wang, S., Huang, X., & Lei, Q. (2024). A performance-based hybrid deep learning model for predicting TBM advance rate using Attention-ResNet-LSTM. *Journal of Rock Mechanics and Geotechnical Engineering, 16*(1), 65–80.
Zhang, Q., Liu, Z., & Tan, J. (2019). Prediction of geological conditions for a tunnel boring machine using big operational data. *Automation in Construction, 100*, 73–83.
Zhang, X. P., Xie, W. Q., Cai, K. Y., Liu, Q.-S., Wu, J., & Li, W. W. (2021). Evaluation of rock muck using image analysis and its application in the TBM tunneling. *Tunnelling and Underground Space Technology, 113*, 103974.
Zhou, X., Gong, Q., Liu, Y., & Yin, L. (2021). Automatic segmentation of TBM muck images via a deep-learning approach to estimate the size and shape of rock chips. *Automation in Construction, 126*, 103685.
Zou, J., Han, J., Zhang, T., & Yang, W. (2020). Experimental investigation and numerical analyses for red sandstone rock fragmentation. *International Journal of Geomechanics, 20*(12), 04020222.